Guiding Synthetic Targets of Anodically Coloring Electrochromes Through Density Functional Theory

Linda Nhon[†], Riley Wilkins[‡], John R. Reynolds[†], Aimée Tomlinson[,‡]*

[†]School of Chemistry and Biochemistry, School of Materials Science and Engineering, Center for Organic Photonics and Electronics, Georgia Tech Polymer Network, Georgia Institute of Technology, Atlanta, GA 30332

[‡]Department of Chemistry & Biochemistry, University of North Georgia, Dahlonega, Ga 30597

[*]Author to whom correspondence should be addressed: aimee.tomlinson@ung.edu

Abstract

Electrochromic devices offer many technological applications, including flexible displays, dimmable mirrors, energy-efficient windows, and others. Additionally, absorbing electrochromic molecular assemblies onto mesoporous metal-oxide surfaces facilitates commercial and manufacturing potential (i.e. screen-printing and/or roll-to-roll processing). These systems also demonstrate synthetic versatility thus making a wide array of colors accessible. In this work, using Time-Dependent Density Functional Theory (TD-DFT), we investigated ten different bi-aryl type molecules of 3,4-ethylendioxythiophene (EDOT) conjugated to various phenyl derivatives as potential anodically coloring electrochromes (ACE). The non-substituted phenylene, hexylthiol-EDOT-phenyl-phosphonic acid, **PA1**, was synthesized and characterized as a means of model validity. **PA1** absorbs in the UV region in its neutral state, and upon oxidation, absorbs within the visible, hence showcasing its potential as an ACE chromophore. The properties of **PA1** inspired the designs of the other nine structural derivatives where the number and position of methoxy groups on the phenylene were varied. Using our DFT treatment we assessed the impact of these modifications on the electronic structures, geometries, and excited-state properties. In particular, we examined stabilization intermolecular interactions (S-O and O-H) as they aid in molecule planarization, thus facilitating charge transport properties in devices. Additionally, destabilizing O-O forces were observed, thereby making some chromophores less desirable. A detailed excited state analysis was performed which linked the simulated UV-Vis spectra to the dominant excited state transitions and their corresponding molecular orbitals. Based on these results the nine chromophores were ranked ergo providing an ordered list of synthetic targets.

Introduction

Electrochromic materials that change color upon an applied electrochemical potential provide access to a plethora of technological and commercial applications by manipulating the electrochromes' transmissive and colored states along with their redox properties. These applications currently range from dimmable visors, eyeglasses, goggles and visors, windows [1–4],

smart windows coupled with energy storage devices [5–10], biochemical and thermal sensors[11,12], flexible displays [13,14], to wearable self-powered and self-cleaning fabrics[15,16]. A variety of electrochromes have been developed to target these colored-to-transmissive applications where one redox state has an absorbance in the visible, thereby appearing colored, and the other redox state has an absorbance outside of the 400-700 nm region to appear colorless.

These materials are often classified as either cathodically coloring (converts to a visibly colored state upon reduction)[17–19] or anodically coloring [20–24] (converts to a colored state upon oxidation). Within these categories, electrochromes are further divided into three main classes of materials: metal oxides[25–27], conjugated polymers[28–31], and molecular dyes[32–34]. While a significant amount of progress has been made in understanding and developing cathodically coloring electrochromic materials such as tungsten oxide[35–38], viologen[39–41], donor-acceptor type polymers[42,43], poly(dioxy)thiophene and their analogues[44–47], anodically coloring materials are considerably less developed.

Figure 1 illustrates the absorbance and redox concepts comparing anodically and cathodically coloring materials. Shown in the dotted blue lines, correctly designed neutral anodically coloring electrochromes (**ACE**s) absorb in the UV region, thereby appearing fully transparent by eye. Upon oxidation, the ACE radical cation will absorb in the visible region appearing colored (solid blue line). In contrast, neutral (or reduced) cathodically coloring materials absorb in the visible (solid magenta line) and their radical cation (or oxidized) state absorb in the NIR to IR region appearing transmissive by eye (dotted magenta line). A caveat to cathodically coloring materials, specifically conjugated polymers, is that the oxidized species of these electrochromes often exhibit an absorbance tailing into the visible region, thus never reaching a fully transmissive state (**Figure 1**). Although molecular cathodically coloring electrochromes have yet to be extensively investigated, it is evident from our previous work that this tailing is absent in the ACE analog.[48] Therefore, pursuing the class of ACE chromophores is a proven strategy to expand the color palette while also asserting high optical contrast and, as such, will be the focus of this study.

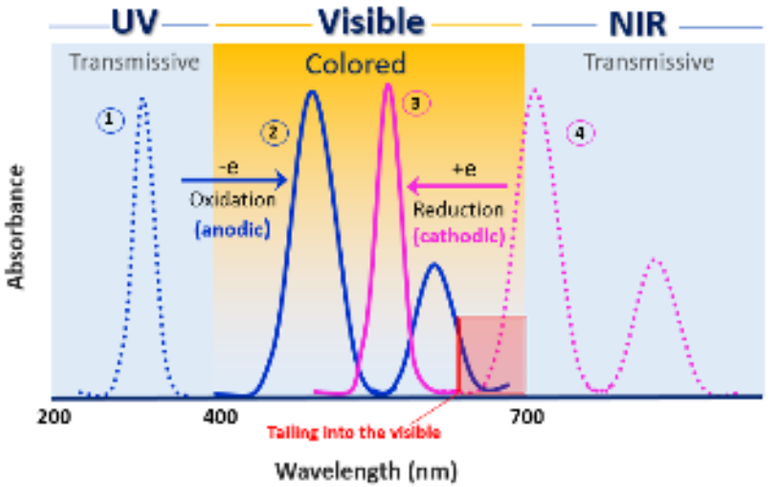

Figure 1. Illustration showing the absorbance profile and redox processes of anodically and cathodically coloring materials. 1.) In its neutral form, anodically coloring material absorbs in the UV. 2.) Absorbance of oxidized species for anodically coloring material absorbs in the visible region. 3.) Reduced (often charge neutral) form of cathodically coloring material absorbs in the visible. 4.) Oxidized form of cathodically coloring material absorbs in the NIR.

Attempts to develop anodically coloring metal oxides including TaOx[49] and NiO[50,51] have been made; however, these materials exhibit low transmissivity in their neutral state. Although these systems benefit from their scalability and redox stability, their electrochromic features are color limited, with brown and blue being the most common. On the other hand, anodically coloring conjugated polymers such as poly-X-dioxypyrrole, where X represents the different N-alkylated substituents on the heterocycle, have been developed and exhibit a wide range of colors in their oxidized state such as red, green, and blue, while also having large energy gaps (~2.0 – 3.4 eV). Although the conjugated polymers offer a variety of colors, their synthesis has been challenging. Alternatively, molecular chromophores provide synthetic versatility advantages, enabling the generation of a wide range of colors[48,52–54]. Molecular systems also have the added benefit of being soluble in both organic or aqueous solvents; therefore, moderate and facile processing techniques such as layer-by-layer electrode assembly or screen printing can be used with these systems.[55–60]

Extensive work conducted on dye-sensitized solar cells (**DSSCs**) and dye-sensitized photoelectrosynthesis cells has shown the potential applications of using molecular chromophores assembled onto transparent conductive electrode surfaces, such as mesoporous nanostructured titanium dioxide (**TiO_2**) and indium tin oxide (**nano-ITO**).[57,61–63] From an electrochromic device (**ECD**) perspective, mesoporous nano-ITO offers several benefits as an

electrode. These advantages include exhibiting high conductivity, high electron mobility, high transparency (owing to its large energy gap: 3.9 – 4.2 eV)[64], and having a large surface area[65]. Compared to a flat surface, nano-ITO's mesoporous morphology and large surface area allow more chromophores to be loaded onto the electrode. Increasing this load amplifies -up to a 1000-fold- the coloration efficiency of the overall molecular assembly relative to a single monolayer of chromophores adsorbed onto a flat surface.[58]

Taking advantage of the metal oxide's mesoporous properties, Sun and co-workers developed a molecular ECD using a phosphonic acid-functionalized viologen adsorbed onto a zinc oxide (**ZnO**) nanowire array. [66] The nanostructured metal oxide increased the dye loading surface area and induced high crystallinity, which allows for faster electron transport. The ECD demonstrated fast switching times (170 and 142 ms for coloration and bleaching respectively for a 1 cm^2 cell) and high coloration efficiency (196 C^{-1} cm^{-2}). These high-performance properties were attributed to the ZnO nanowires. Recently, Alan and co-workers developed and characterized an electrochromic self-assembled monolayer using a terpyridine-based chromophore, L, deposited onto screen-printed nano-ITO substrates via chemisorption. The nano-ITO electrodes were made by sintering either ITO-30 or ITO-50 nanoparticles onto the glass. The molecule was rendered redox-active upon intercalation by an iron or ruthenium ion, thereby forming the electrochromic (**EC**) substrates- Fe-L|ITO-30(50) or Ru-L|ITO-30(50) monolayers. These EC materials demonstrated color differences at two states, for which their optical density changed as a function of pulse width (5-60 s). Although ITO-50 films had slightly higher surface areas (30.0 m^2/g), their overall ECD performance was inferior to that of ITO-30 (10.2 m^2/g) films, which the authors attributed to the presence of hydroxyl defect sites that impeded the formation of the metal-chromophore complexes. Despite the slight differences in surface chemistry, the ECDs made using either type of screen printed ITO substrates exhibited long-term stability. Negligible optical deterioration was observed for both ITO-30 and ITO-50 devices during 1500 chronoabsorptometric switching cycles within 48 h. These devices also demonstrated fast switching speeds, where the ECDs could be switched to 3V in under five sec.[59]

Moreover, the Irish start-up company, Ntera, capitalized on a similar assembly technique by commercializing screen printed ECDs, for which over 20 different patents were published to develop their display technology.[67] In general, their ECD consists of a transparent layer positioned on the viewer side, a coloring electrode or chromic layer, a separator, a second electrode, an electrolyte permeating throughout the ECD, and a back layer positioned on the backside of the display.[68] Each layer is deposited on top of each other in sequential order. In Ntera's latest patent, they stated that the preferred electrode embodiment would be constituted

of a mixture of semiconducting nanoparticles, such as titanium dioxide (**TiO_2**), onto which electrochromes have been adsorbed. Currently, their ECDs use cathodically coloring electrochromes such as viologens and its structural derivatives to achieve different hues of blue. Differing from prior art, this company can also screen print the conductive layer in the lateral direction, thereby creating a working electrode with conductivity in three dimensions. They claim this feature has not been previously achievable.

Although Ntera has made advancements in designs of ECDs and manufacturing techniques of electrodes, their displays are currently limited by the availability and array of colors provided by the chromophores, especially ACEs. Even though more than eight classes of cathodically coloring materials have been investigated, Ntera only explored two types of ACE molecules; thiophenazine and diphenylaminobenzyl type compounds. Additionally, besides the cathodically coloring viologens and its derivatives, the ECDs containing these chromic layers have yet to be commercialized. For all screen printed ECDs, the electrochromes possessed a phosphonic acid anchoring group that tethered the molecules onto the metal oxide (**MO_x**) substrate.

While the aforementioned work made significant progress in showcasing the ease in fabrication and stability of their molecular ECDs; they are still limited by the type of discrete electrochromic molecules available for further investigations of molecular assemblies prepared on nanostructured conducting substrates. Motivated by the above work and our recent progress in developing ACE molecules[48], this study expands on the ACE design paradigm. Here, 4-(7-(hexylthio)-2,3-EDOT-phenyl-phosphonic acid, **PA1**, was synthesized, and its experimental optical properties were compared to the corresponding theoretical results, showing nearly identical matching of the lambda max (**λ_{max}**) values. Encouraged by these results, we computationally investigated ten molecules composed of **PA1**'s EDOT-X-phenylene structural motif, where X is indicative of the number and location of methoxy groups on the phenyl ring. In the current structures, a methylene phosphonic acid group is installed at the *para*-position, whose role is to tether the chromophore onto a MO_x surface. In this work, we use Time Dependent-Density Functional Theory (**TD-DFT**) to elucidate the structure-property relationship of this new set of ACE chromophores.

When paired with the correct functional and basis-set[69], TD-DFT simulations offer many advantages to understanding fundamental inter- and intra-molecular interactions. This approach has been utilized to develop new materials in organic electronics[70–72], such as DSSCs[73–75], organic photovoltaics[76,77], perovskites[78], and others. TD-DFT calculations provide information on the molecule's ground-state optimized geometry, as well as excited-state electronic transitions

and their corresponding oscillator strengths (***f***).[79] This level of theory can also generate UV-Vis spectra of molecules in both the neutral and radical cation states. These spectroscopic predictions are essential for ACE applications because it provides qualitative color prediction relative to the electrochromes' hue and saturation.[48] In order to set a framework to guide future synthetic approaches, we have undertaken a theoretical study of the geometry and excited states of both the neutral and radical cation forms of these EDOT-*X*-phenylene systems.

Results and Discussion:

A. Motivation for Calculations: PA1 Experimental Results

Scheme 1 outlines the synthetic route towards the **PA1** chromophore. An unsubstituted EDOT was functionalized with a hexyl thiol ether sidechain at the 2'-position giving **1** with moderate yields using n-BuLi as the lithiation reagent and a dihexyldisulfide as the electrophile. Compound **1** was stannylated with trimethyltinchloride to give compound **2** at relatively high yields, and **2** was coupled to the commercially available halogenated aryl group, 1-Bromo-phenyl-4-phosphonate. Stille cross-coupling conditions using $Pd_2(dba)_3$ as the catalyst and P(*o*-tol)$_3$ ligands in toluene were employed to give the phosphonate form chromophore, **PA1E**. To expose the phosphonic acid, **PA1E** was deprotected in a mixture of bromotrimethylsilane and dichloromethane in methanol to produce **PA1**. Details of synthetic procedures and characterizations are provided in the supporting information. The phosphonate group on **PA1E** renders this molecule highly soluble in organic solvents; therefore, characterizations of **PA1E** used common optical and electrochemical techniques. It was hypothesized that **PA1E** and **PA1** should exhibit similar optical properties because the ethyl groups on the phosphonate should only influence the solubility of the chromophore without impacting the spectral or redox properties.

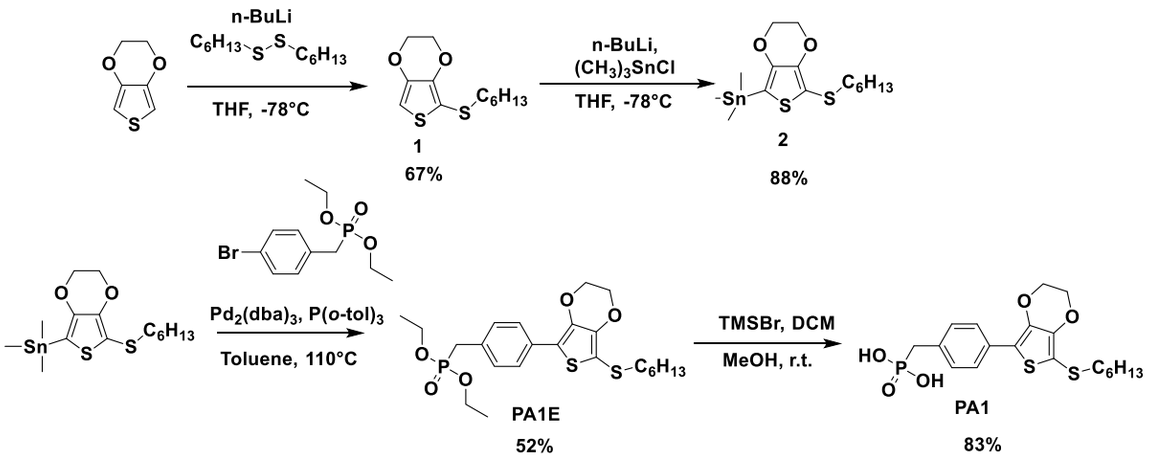

Scheme 1. Synthetic route towards **PA1E** and **PA1**.

Figure 2A shows the absorbance spectra of the neutral and oxidized forms of **PA1E** (in solution) and **PA1** (as a film)**.** The neutral spectrum of **PA1E** was generated in dichloromethane (**DCM**), whereas that of **PA1** was taken as a film adsorbed onto nano-ITO, **nano-ITO|-PA1**. The radical cation spectra of **PA1E** were collected via spectroelectrochemical (**spec-echem**) methods (after performing chemisorption in 1 mM solution of chromophore/DCM) in a 0.5 mM $TBAPF_6$/ DCM electrolyte using an optically thin layer electrode (**OTTLE**) with a Pt mesh working electrode, Pt flag counter electrode, and Ag/AgCl reference electrode. The radical cation film spec-echem absorbance of **PA1** was also taken in a 3-electrode cell set-up, with the working electrode being nano-ITO|-PA1, and the same counter and reference electrodes as those used for **PA1E**. The measurements were also produced in a $TBAPF_6$ electrolyte solution at a concentration of 0.5 mM in DCM after soaking in 1.0 mM concentration of **PA1** in DCM. Both oxidized spectra were taken at +1.0 V vs. Ag/AgCl. Both chromophores in their neutral state exhibit a λ_{max} of 320 nm and share an onset of absorbance at 367 nm. As shown in the yellow box, both **PA1** and **PA1E** lie strictly in the UV region in their neutral form (**Figure 2A**). Their oxidized forms also show overlap between their λ_{max} peaks at 449 nm and 645 nm. These results suggest that the phosphonate derivative in solution are reliable indicators for how the phosphonic acid chromophore will behave optically on film; however, aggregation effects cannot be considered here.

Furthermore, to characterize their redox properties, electrochemical measurements using cyclic (**CV**) and differential pulse voltammetry (**DPV**) were taken of **PA1E** in DCM and **PA1** adsorbed onto nano-ITO. Both chromophores were performed in the same 3-electrode cell set-up as described above for their respective spec-echem measurements. **Figure 3A** shows the CV and DPV scans of **PA1E** in solution. The CV of **PA1E** exhibited an electrochemically reversible

oxidation curve having an oxidation potential ($\mathbf{E_{ox}}$) at 1.01 V vs. Ag/AgCl and a half-wave potential ($\mathbf{E_{1/2}}$) at 0.96 V. The CV's $E_{1/2}$ value also matches with that of **PA1E** DPV oxidation peak ($\mathbf{E_{ox}^{peak}}$) as shown in **Figure 3A**. **Figure 3B** demonstrates nano-ITO|-**PA1** films withstand repeated electrochemical cycling by maintaining its CV shape up to 50 cycles. Nano-ITO|-PA1 has an $E_{1/2}$ at 0.92 V vs. Ag/AgCl. The **PA1** film CV and **PA1E** in solution share similar shape and oxidation potentials, thus follow the trends observed above.

In order to test the validity of our model predictions, calculated spectra were generated for the neutral and radical cation states of both chromophores. Previously, we have found an excellent correlation to the experimental work by utilizing the mPW1PBE functional[80–82] coupled with the cc-PVDZ basis set with DCM inclusion through the conductor polarizable continuum model (**CPCM**).[48,83] Here we have utilized this treatment to generate frequency verified optimized geometries, frontier molecular orbitals (**FMOs**) and the lowest-lying 15 excited states which produced the simulated spectra. **Table S1** provides a summary of both **PA1** and **PA1E** calculated excited state transitions for both neutral and radical cation states. There is a strong agreement between the calculated and experimental UV-Vis absorption spectra for **PA1** (**Figure 2B)**. For example, the spectra for the neutral molecule have nearly identical overlap (**Figure 2B**, dotted lines). Moreover, for the radical cation form, both the simulated and experimental spectra indicate the higher energy (**HE**) peak has the strongest intensity compared to the lower energy (**LE**) one. Excited-state analysis reveals that the radical cation's peak, at 424 nm, is a result of the dominant electronic transition from the singularly occupied molecular orbital with an electronic spin up **($\mathbf{S_\alpha}$)** to the lowest unoccupied molecular orbital ($\mathbf{L_\alpha}$), $\mathbf{S_\alpha \rightarrow L_\alpha}$, with a moderately strong oscillator strength ***(f)*** of 0.54. The LE peak was generated by the singularly occupied molecular orbital with an electronic spin-down, $\mathbf{S_\beta - 1 \rightarrow L_\beta}$ transition, and a weak *f* value of 0.21. These calculations provide insight into the difference in absorbance intensities observed between the two curves in **PA1** radical cation spectra. While the calculations provide accurate approximations of the λ_{max} for **PA1**, the width and sharpness of the LE band lacks substantial overlap. This issue coupled with the small LE oscillator strength make color prediction a challenge for these discrete conjugated molecular systems. An examination of the FMOs exhibit nearly identical images for the orbitals involved in the four major excited state transitions, ES3, ES4, ES5, and ES6 (**Figure S2**)**.** In terms of geometry, both have similar S-C-C-C dihedral angles with **PA1E** being slightly more twisted, ~5°, than the acid derivative. Overall, these results not only suggest that the optical properties of the phosphonate and phosphonic acid derivatives should be comparable, but also provide validity to the DFT model for these systems.

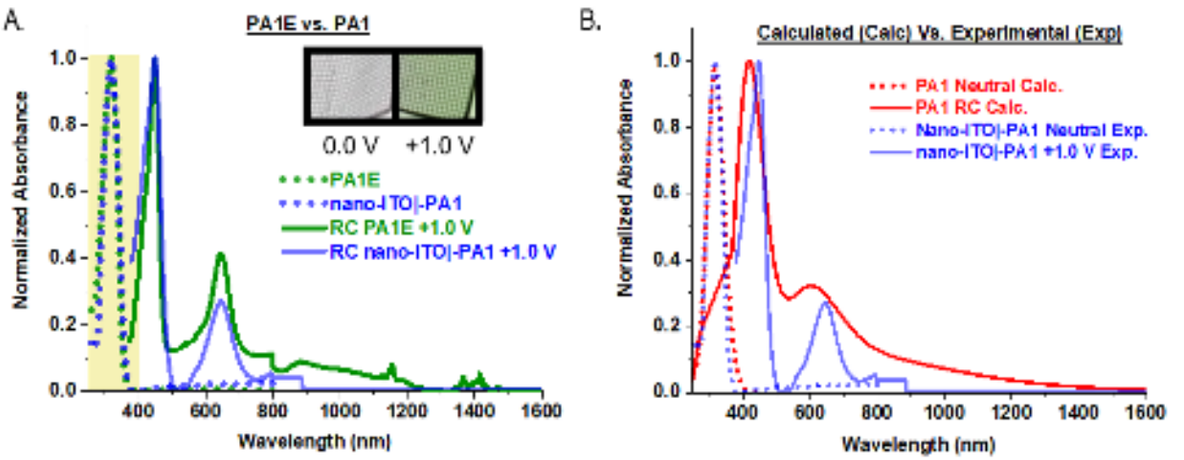

Figure 2. A.) Absorbance spectra for both neutral and radical cation (RC) forms of **PA1E** and **PA1**. **PA1E** experimental was taken in dichloromethane and PA1 was taken in a film on nano-ITO. The experimental spectra for **PA1E** radical cation absorbance was collected under a constant flow of inert Ar atmosphere in 0.5 mM $TBAPF_6$/ DCM electrolyte using an optically thin layer electrode (OTTLE) with a Pt mesh working electrode, Pt flag counter electrode, and Ag/AgCl reference electrode. The **PA1** experimental spectra for the radical cation absorbance were collected on film with the chromophore adsorbed onto nano-ITO (after soaking in a 1 mM solution of PA1 in DCM) in 0.5 mM $TBAPF_6$/ DCM electrolyte, with the working electrode being nano-ITO|-PA1, Pt flag counter electrode, and Ag/AgCl reference electrode. **Inset**: Image of **PA1E** taken in the OTTLE at extreme potentials. **B.)** Calculated spectra (red) of the neutral and radical cation states of PA1 overlapped with its experimental absorbance spectra (blue).

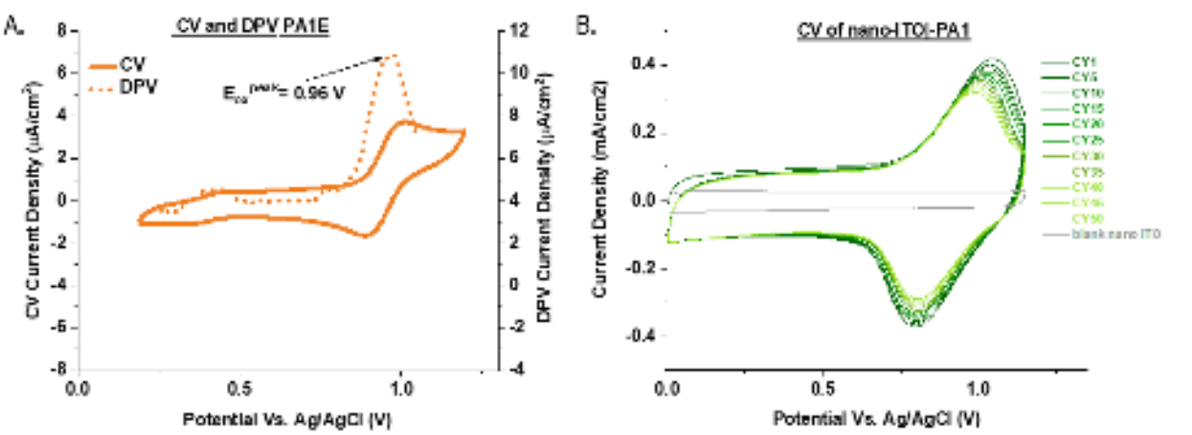

Figure 3. A.) Cyclic voltammetry (CV) and differential pulse voltammetry (DPV) scans of **PA1E** in dichloromethane using 0.5 M $TBAPF_6$ as the electrolyte solution at a concentration of 0.5 M. using Ag/AgCl reference electrode, Pt button electrode, and Pt Flag counter electrode. CV was done at a 50 mV/s scan rate. DPV was performed using a 2 mV step size, 80 ms step time and 50 mV pulse amplitude. **B.)** Electrochemical stability measurements using CV of **PA1** adsorbed onto nanoITO (nanoITO|-PA1) at a scan rate of 50 mV/s using the film as the working electrode, Ag/AgCl reference electrode, and a Pt flag counter electrode.

Based on optical and redox properties, **PA1** is a promising ACE chromophore. Previously, we developed a family of ACE molecules, whose structural motif was composed of a bi-aryl ring consisting of 2-thiomethyl-EDOT conjugated to a 4-methoxy-benzene.[48] The electron density was manipulated in this family by adding either electron-withdrawing or electron-donating substituents to the phenyl ring's *meta*-positions. Structure-property analysis of the radical cation revealed that increasing electron richness promotes the lower energy excited state transition of $\mathbf{S_\beta} \rightarrow \mathbf{L_\beta}$ rather than the higher energy $\mathbf{S_\beta - 1} \rightarrow \mathbf{L_\beta}$ as observed in the electron-poor system. The differences in dominant excited state transitions are observed as a spectral shift in the LE peaks', where the $\mathbf{S_\beta} \rightarrow \mathbf{L_\beta}$ transition contributes to a red-shift in the absorbance. The ability to manipulate excited state transitions in odd electron systems by simply changing the neutral molecule's molecular structure is a promising strategy to assert control over the radical cation absorbance spectra, hence allowing for greater color control and optical contrast between the neutral and oxidized states.

In comparison to previous ACE molecules, **PA1** exhibits similar optoelectronic properties and excited state transitions to the electron-poor molecule, 2-methoxy-5-(7-(methylthio)-ethylene-dioxythiophene-benzonitrile, **ACE1**, where a cyano functional group is attached to the phenyl ring.[48] However, unlike the previous work, **PA1** also has the ability to adsorb on MO_x electrodes, thus can be integrated into film-based ECDs for solid-state applications. Motivated by this, we sought to develop a new class of **PAX** adsorbable chromophores using in-depth TD-DFT calculations to understand their structure-property relationship.

B. Rational Design for PA1-PA10 Chromophores

Ten bi-aryl EDOT conjugated to an X-phenyl-ethyl-phosphonic acid, where X denotes the position and number of methoxy, OCH_3, groups on the phenyl ring (**PA1-PA10**), were examined. **Scheme 2** shows the generic structure of the **PAX** core, chemical structures, abbreviated name, and shortened nomenclature for the ten molecules. In general, the family starts with a 2,3,5,6-unsubstituted *para*-phenylene in **PA1**, and OCH_3 groups are then incrementally added onto the ring at different positions to generate the full family of structures. To illustrate, **PA2** and **PA3** are constitutional isomers, each containing one OCH_3 on the phenylene, **PA4-PA7** all have two OCH_3, **PA8**, and **PA9** have three OCH_3, and lastly, **PA10** possesses four OCH_3 groups. The short conjugation length in the bi-aryl ring system ensures that the molecules will have a large energy gap (> 3.0 eV); thus, their neutral state will absorb within the UV region. The methyl thiol-ether and OCH_3 functional group provide electron richness and steric interactions. Additionally, the electron richness should influence the FMO energy levels and possibly the excited state transition of the chromophore. The non-electrostatic interactions between the O-S, O-H, and O-O atoms

will have either structural stabilization or destabilization effects, which may shift the chromophores' neutral and oxidized state absorbance curves. Lastly, the phosphonic acid offers adsorption capability onto the nano-ITO surface.

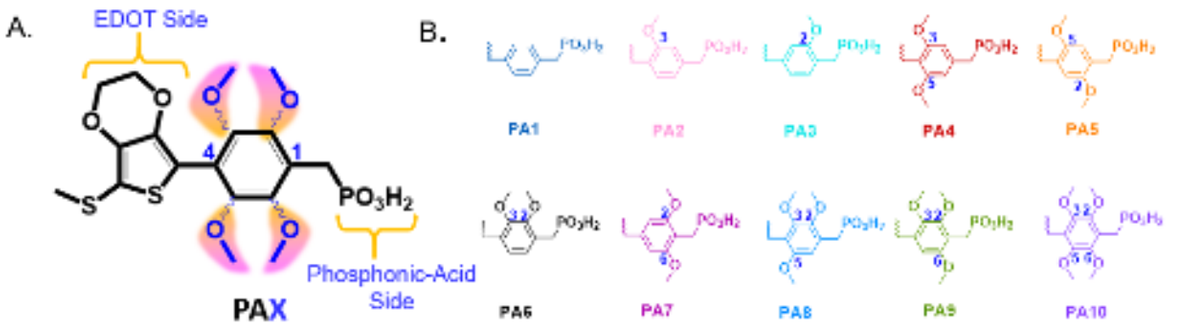

Scheme 2. **A.)** General chemical structures of PAX family. **B.)** Chemical structures of PAX family with their associated acronym and abbreviated name.

C. Neutral Analysis of PAX Chromophores

Upon optimization and excited state generation, the highest occupied molecular orbital (**HOMO**), the lowest unoccupied molecular orbital (**LUMO**), the optical energy gap ($\mathbf{E_g}$), and the geometry (phenylene ring dihedral angles with EDOT and PA and distances between adjacent atoms) were examined as shown in **Table 1**. **SI Scheme S2** shows the chemical structures of the chromophores in the neutral state coupled with their dihedral angles and atomic distances [O-O (D_{1O} = distance between EDOT and adjacent methoxy O-atoms or D_3 = distance between methoxy and adjacent hydroxyl O-atoms from phosphonic acid group), O-H (D_{1H} = distance between EDOT O-atom and benzene H-atom), or O-S (D_2 = distance between EDOT S-atom and adjacent methoxy O-atom)]. To provide a sense for the impact these distances may have on the structure properties they will be compared to the corresponding van der Waals radii (vdW) [O-O ~2.70, O-H ~2.40, O-S ~3.4 Å].[84] The UV-Vis spectra and the corresponding excited-state analysis for both the neutral and radical cation states were also examined (**Figure 4** and **Figure 5**). There was no discernable trend for the dihedral angle between the phenylene and the phosphonic acid and therefore will not be discussed further.

Table 1. A comparison of the neutral PAX molecules. HOMO, LUMO, and energy gaps and the geometric measurements for each of the 10 PAX systems. A schematic of the geometric measurements of all electrochromes are shown at the top. *(A larger version of the chemical structures is given in SI Scheme S2)*

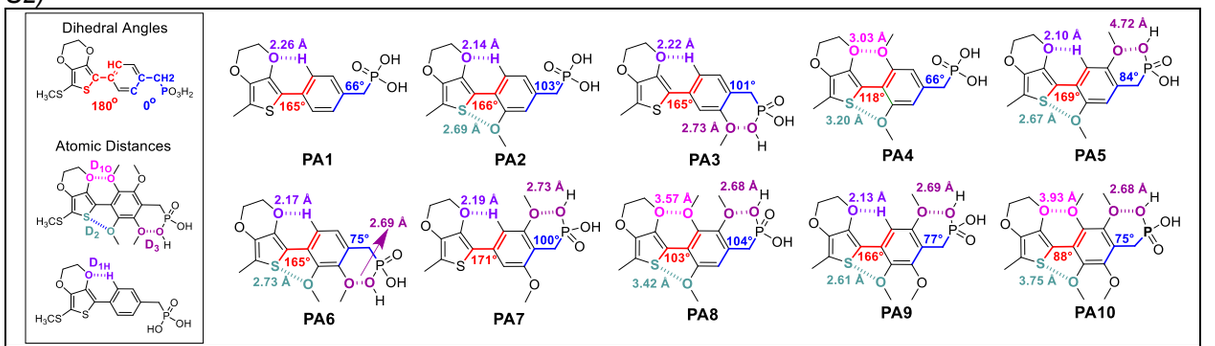

ACE	HOMO (eV)	LUMO (eV)	Energy gap (eV)	Dihedral Angles (°)		Atomic Distances (Å)			
				S-C-C-C	C-C-C-P	D_{1O}	D_{1H}	D_2	D_3
PA1	-5.93	-1.40	3.88	165.3°	66.0°	N/A	2.26	N/A	N/A
PA2	-5.72	-1.28	3.78	165.6°	103.2°	N/A	2.14	2.69	N/A
PA3	-5.94	-1.46	3.83	165.2°	100.6°	N/A	2.22	N/A	2.73
PA4	-5.93	-0.92	4.21	118.1°	65.2°	3.03	N/A	3.20	N/A
PA5	-5.57	-1.13	3.60	168.5°	83.6°	N/A	2.10	2.67	4.72
PA6	-5.90	-1.41	3.82	165.2°	75.1°	N/A	2.17	2.73	2.69
PA7	-5.92	-1.48	3.80	170.8°	99.9°	N/A	2.19	N/A	2.73
PA8	-6.21	-0.86	4.46	103.1°	104.2°	3.57	N/A	3.42	2.68
PA9	-5.85	-1.41	3.78	166.1°	76.7°	N/A	2.13	2.73	2.69
PA10	-6.33	-0.76	4.76	88.0°	74.8°	3.93	N/A	3.75	4.89

C1. PA1-PA3 Neutral States

The HOMO for **PA2** (EDOT-3-Methoxy-B-PA) was 0.21 eV higher than **PA1** and **PA3** (EDOT-2-Methoxy-B-PA), even though **PA2** and **PA3** are constitutional isomers. On the other hand, **PA3** and **PA1** (EDOT-B-PA) possessed nearly identical HOMO, LUMO, and E_g values (**Table 1**), thereby suggesting the impact of a methoxy group on the phosphonic acid side is energetically insignificant. Additionally, the E_g for **PA2** was 0.10 eV and 0.05 eV lower than **PA1** and **PA3**, respectively. This smaller E_g is likely due to the S-O stabilization effect between the O-atom in the OCH_3 on the phenyl ring to the S-atom in the neighboring EDOT, giving a short O-S atomic distance of 2.69 Å (less than vdW of 3.4 Å).[84] Finally, as all three of these systems possessed nearly identical S-C-C-C dihedral angles (0.4° difference), the presence of a single methoxy group on either side of the phenylene does not result in a steric interaction with the adjacent EDOT ring or phosphonic acid group. Additionally, destabilizing the HOMO energy levels are also desirable for these chromophores because it suggests their electrochemical oxidation potential will also decrease.

C2. PA4-PA7 Neutral State

Next, the constitutional isomers **PA4** (EDOT-3,5-Dimethoxy-B-PA), **PA5** (EDOT-2,5-Dimethoxy-B-PA), **PA6** (EDOT-2,3-Dimethoxy-B-PA), and **PA7** (EDOT-2,6-Dimethoxy-B-PA), whom all share the dimethoxy benzene core were examined (**Table 1** and **Scheme S2**). For **PA4**, the addition of a second methoxy at the 5'-position the phenyl ring of **PA2** generated an increase in both dihedral angle and D_2 (S-O, less than vdW) separation of 48° and 0.51 Å, respectively. Additionally, there was a 0.21 eV stabilization in the HOMO level while the LUMO level was raised by 0.36 eV thereby leading to a 0.43 eV increase in the band gap. A similar comparison between **PA3** and **PA7** shows little difference in the HOMO and LUMO levels and the energy gap which is not surprising as there was only a 0.05 Å reduction in D_{1H} (O-H, less than vdW) coupled with a 5.3° loss of torsional strain. In the case of PA5, the other methoxy group (placed *trans* to that of either PA3 or PA2) produced the highest HOMO and the lowest energy gap of the entire PA series, which was the result of stabilization provided by D_{1H}, and D_2 (both less than vdW) as well as a complete lack of destabilization from D_3 given it was greater than the van der Waals distance, Unfortunately, this small energy gap size is further evident in the UV-Vis spectra of **PA5**, where there is an unfavorable absorption in the visible region (**Figure 4**). On the other hand, affixing a second methoxy group *cis* (**PA6**) to the **PA2** group led to decreases in both the HOMO (0.18 eV) and LUMO (0.14 eV) levels as well as a slight energy gap increase (0.04 eV) possibly the result of the 0.04 Å decrease in D_2 (less than vdW). Finally, comparing the four isomers indicates that placing methoxy groups on the EDOT side leads to a significant increase in the dihedral angle and the energy gap (see **PA4** versus the rest). Alternatively, **PA7**, compared to **PA1** and **PA3**, suggests that affixing methoxy groups to the phosphonic acid side does not significantly impact the electronic nor the geometric properties of these neutral systems.

C3. PA8-PA10 Neutral State

The last set of neutral molecules to be compared are **PA8** (EDOT-2,3-5-Trimethoxy-B-PA), **PA9** (EDOT-2,3,6-Trimethoxy-B-PA), isomers sharing the trimethoxy benzene core, and **PA10** (EDOT-Tetramethoxy-B-PA). For **PA8**, the third methoxy group was placed on the phosphonic acid side of **PA4** producing a destabilization of the HOMO (0.28 eV), a LUMO increase (0.06 eV) and a widening of the energy gap (0.25 eV) which resulted in an absorbance blue-shift relative to **PA4**. Additionally, **PA8** also exhibited a 0.54 Å increase in D_{1O} which was considered insignificant since this separation was greater than the vdW distance. These changes were generated by the proximity of the two methoxys *ortho* to the EDOT side which caused a 15° increase in the twisting of the S-C-C-C dihedral angle.

On the other hand, affixing a second methoxy on the EDOT side of **PA7**, thereby giving rise to **PA9**, effectuated a minor change of +0.07 eV, +0.07 eV, -0.04 eV, and 0.05 Å in the HOMO, LUMO, energy gap, and O-O distance (D_3, greater than vdW hence insignificant), respectively. These findings provide further support that the addition of substituents on the phosphonic acid side has minimal impact on the system properties. Moreover, the stabilization provided by the 2.73 Å in D_2 (S-O interaction distance < vdW) appeared to be inconsequential given these results. Finally, **PA10** containing the tetramethoxy phenyl core exhibited the lowest or most stabilized HOMO level, highest LUMO level, widest energy gap, largest adjacent atom separations (except for D_3 < vdW), as well as the most twisted dihedral angles due to the steric effect caused by the four methoxy groups. Finally we examine the geometric results of the entire series considering the planarity (using S-C-C-P), stabilization (using D_{1H} and D_2) and destabilization (using D_{10} and D_3) effects from the most to least structurally desirable (see **Table S3**): **PA5**, **PA2**, **PA9**, **PA6**, **PA7**, **PA1**, **PA4**, **PA3**, **PA8**, **PA10**.

C4. Neutral Absorbance: Excited State Analysis for PA1-PA10

The neutral UV-Vis spectra were simulated (**Figure 4**) along with a detailed analysis of the significant excited state contributors (those which possessed *f* values greater than 0.1000, **Table S2**). With the exception of **PA5**, there was little tailing into the visible suggesting the remaining systems will likely possess the desired transmissivity needed for the ACE neutral state. Regardless, the trends for all ten chromophores will be discussed and compared. The lowest excited (ES1) for all but **PA10** were the result of the HOMO (H) to LUMO (L) transition. There was an 8 nm or less λ_{max} difference between **PA1**, **PA2**, **PA3**, **PA6**, **PA7**, and **PA9**. Comparatively, **PA5** was red-shifted by 25 nm while **PA4**, **PA8**, and **PA10** all indicated a hypsochromic shift of 26 nm, 42 nm, and 60 nm, respectively. Both trends are due to steric interactions leading to an increase (**PA5**) or decrease in planarity (most to least: **PA4** > **PA8** > **PA10**). The lack of planarity for these latter three resulted from the two methoxy groups on the EDOT side with a small contribution from additional groups placed on the phosphonic acid side. Additionally, this increased out-of-plane twist could be the culprit behind the H - 3 $\rightarrow$ L + 1 transition for the ES1 of **PA10**.

For the second excited state, the wavelength of absorption for **PA1**, **PA3**, **PA5**, **PA6**, and **PA9** differed by 7 nm and was due to the H – 1 to L transition. A comparison between **PA8** and **PA10** indicated only a 2 nm λ_{max} difference which is interesting given their H – 1 levels were excited to two different levels, the L and the L+1, respectively. The second significant excited state for **PA2**, **PA4**, and **PA7** occurred at a much higher energy and as such are too blue-shifted

relative to the visible spectrum to be considered. Furthermore, as we are primarily interested in the states which are in close proximity to the visible region, we will not discuss in detail the remaining three states for these electrochromes. Furthermore, this second excitation is less significant for the transmissivity of the neutral state given the lowest wavelength of absorption in this series was 295 nm (**PA5**).

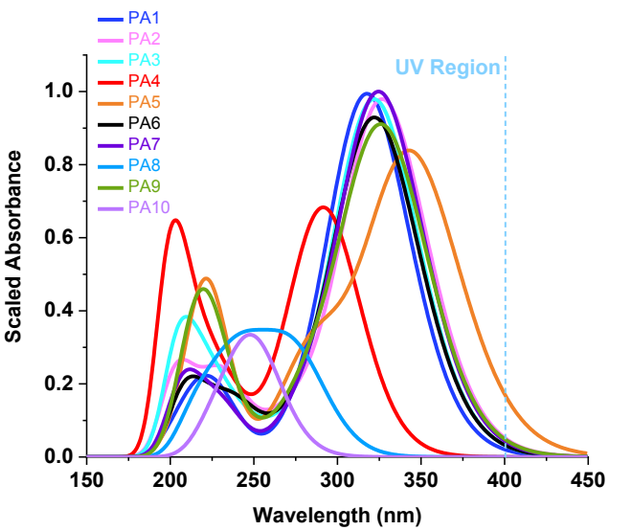

Figure 4. Neutral UV-Vis spectra for all ten chromophores where absorbance was normalized by both the largest absorbance as well as the largest oscillator strength. The dashed blue line is indicative of the start of the visible spectrum.

D. Radical Cation Analysis on PA1-PA10 Chromophores

Next, we performed the same treatment on the radical cation version of each of these electrochromes. **Scheme S3** shows the radical cation molecular structures of **PA1**-**PA10** with their respective dihedral angles and atomic distances, as tabulated in **Table 3**. For the excited state analysis, these chromophores were subdivided, and their structure-property (geometry, D_2 (O-S), D_{1O}/D_3 (O-O), D_{1H} (O-H) relationships were compared within each group: Group 1: **PA1**-**PA3**, Group 2: **PA4**- **PA7**, and Group 3: **PA8**- **PA10**. Overall, the dihedral angle between the two aryl groups (S-C-C-C) became more planar in going from the neutral to the oxidized state as the radical cations adopt the quinoidal structure. In general, inducing planarity in the chromophores is desirable for stabilizing the radical cation state and improving electron transport properties within ECDs.

Table 2. A geometric comparison of the radical cation form of the 10 **PAX** molecules. A representation of the geometric measurements of all electrochromes are also shown. *(A larger version of the chemical structures is given in SI Scheme S3).*

ACE		Dihedral Angles (°)		Atomic Distances (Å)			
		S-C-C-C	C-C-C-P	D_{1O}	D_{1H}	D_2	D_3
PA1	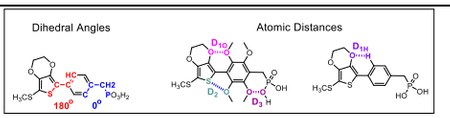	176.1°	75.9°	N/A	2.19	N/A	N/A
PA2		177.6°	111.2°	N/A	2.09	2.59	N/A
PA3	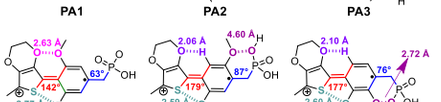	177.0°	99.3°	N/A	2.16	N/A	2.77
PA4		142.4°	63.0°	2.63	N/A	2.77	N/A
PA5		179.5°	87.2°	N/A	2.06	2.59	4.60
PA6		176.5°	75.8°	N/A	2.10	2.60	2.72
PA7	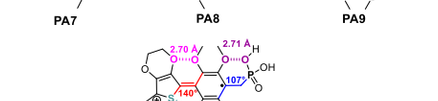	178.2°	98.2°	N/A	2.15	N/A	2.78
PA8		138.5°	151.3°	2.69	N/A	2.82	2.70
PA9	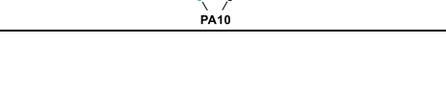	174.8°	77.4°	N/A	2.08	2.61	4.76
PA10		140.1°	106.5°	2.70	N/A	2.82	2.71

D1. Group 1: PA1, PA2, and PA3 Radical Cation States

All three molecules possess an O-H distance (D_{1H}), which differed by 0.10 Å and fell within the approximate vdW distance of ~2.40 Å for a typical O-H interaction.[84] Additionally, there is only a 1.5° dihedral S-C-C-C angle difference for this group (**Table 2** and **Scheme S3**). **PA2** exhibited a 2.59 Å separation between the sulfur on EDOT and the oxygen on the phenylene (D_2), which is less than 3.4 Å (the vdW distance for S-O interaction).[84] The OCH_3 group on **PA3** does not appear to provide structural stabilization whereas it does seem to induce conformational locking in **PA2**. While both **PA1** and **PA3** have an O-H interaction, the presence of the OCH_3 group on **PA3** increases the molecule's chance of having an O-O repulsion (D_3) between the phosphonic acid and the OCH_3 group. This slight repulsion contributes to the dihedral angle difference between **PA3** and the other two chromophores. Overall, the planar conformation, S-O, and O-H interactions make **PA2** the most geometrically stable molecule (for favorable charge transport properties) in Group 1 (**PA2**, **PA1** then **PA3**).

D2. Group 2: PA4-PA7 Radical Cation States

Next, constitutional isomers **PA4**-**PA7** from Group 2 were examined. Similar to the trends observed in their neutral structures, **PA5**, **PA6**, and **PA7** all have nearly planar S-C-C-C dihedral angles, while **PA4** is contorted out of plane to ~142°. This torsional strain in **PA4** occurs in spite

of the stabilization contribution from the 2.77 Å D_2 (within the vdW radii for S-O) as it is due to the proximity of the two OCH_3 groups on the EDOT side as well as the destabilization from the 2.63 Å D_{1O} (within the ~2.70 vdW distance for O-O interactions).[85] Both **PA5** and **PA6** show O-H and S-O interactions, sharing similar D_{1H} and D_2 distances **(Table 2** and **Scheme S3)**. Moreover, while both **PA4** and **PA7** have their OCH_3 group *meta* to each other, as previously noted, the OCH_3 groups placed on the phosphonic acid side (**PA7**) generate a reduced steric effect in comparison to those affixed to the EDOT side (**PA4**). Although both **PA7** and **PA6** possessed slight O-O repulsion (D_3), the second OCH_3 group in **PA6**, unlike in **PA7**, also participates in an S-O interaction thereby inducing molecular stability. Thus, **PA6** would be a more favorable molecule to study than **PA7**. In sum, the conformational analysis on Group 2 suggests that **PA5** is the most geometrically favorable because it has both O-H and S-O interactions and lacks O-O repulsion. Taking all of these trends into consideration, the suggested order of synthesis would be **PA5**, **PA6**, **PA7**, and finally **PA4**.

D3. Group 3: PA8- PA10 Radical Cation States

The last group in the series, Group 3, consists of **PA8**, **PA9**, and **PA10**, in which **PA8** and **PA9** are constitutional isomers with three OCH_3 on the phenylene, and **PA10** has four OCH_3. For this set, only **PA9** is planar with an S-C-C-C dihedral angle of 175° while **PA8** and **PA10** are twisted out of plane by 41° and 40°, respectively. The planarity induced in **PA9** is attributed to the O-H and O-S interactions in which both D_{1H} and D_2 fall within their respective vdW radii distances. Although **PA10** and **PA8** also have an O-S interaction, the torsional strain is partly caused by O-O repulsion interaction where D_{1O} is 2.69 Å and 2.70 Å (within vdW), respectively. This phenomenon is similar to the earlier observation made in **PA4** and is again reflected in the slightly longer O-S distance, with D_2 being 2.82 Å for both molecules. Constitutional isomers, **PA8** and **PA9**, both have S-O stabilization as well as O-O repulsion on the phosphonic acid side. Like the comparison between **PA4** and **PA7**, the additional O-O interaction on the EDOT side, coupled with this steric effect, produces an even more significant torsional strain for **PA8** than was found for **PA4**. Finally, even though **PA10** has the most O-O repulsion, the addition of the fourth OCH3 does not cause a considerable geometric change relative to **PA8**, given there is only a 1° difference in their respective dihedral angles. From this group, **PA9** is the most favorable due to its planarity, then **PA8** and **PA10** follow with similar weight in favorability based on their steric effects, thus **PA9**, **PA8** then **PA10**. Incorporation of the geometric findings as well as the stabilization results produces an overall ranking from most to least structurally stable of (see **Table S4**): **PA5**, **PA2**, **PA9**, **PA6**, **PA7**, **PA1**, **PA3**, **PA4**, **PA10**, **PA8**. This order is a replication of

the one found for the neutral state with the exception of a switch between **PA6** and **PA7** as well as **PA8** and **PA10**.

E. Radical Cation Absorbance: Excited State Analysis

To gain further insight, we generated both the simulated UV-Vis (**Figure 5**) and a corresponding detailed excited state analysis (**Table 3**) in which all the significant excited state transitions ($f > 0.1$) have been paired with their corresponding frontier molecular orbitals (FMOs). Unlike the neutral spectra, the radical cation absorbance falls within the visible region. Here, the *f* values are related to the saturation of the resultant color, therefore we will utilize this in order to identify the most promising electrochromes.[86] Each transition was generated by the excitation of a spin down (S_β) or up (S_α) electron from the set of singly occupied molecular orbitals (SOMOs) to the LUMO (L) set. Additionally, we have segmented these transitions according to the identity of the FMOs from which they originated and finished. As a consequence, this treatment led to four different excited states (ES1, ES2, ES3, and ES4) which spanned a 656 nm spectral range. Only four molecules show ES1 transitions, λ_{max} ranging from ~600-1050 nm. All ten chromophores exhibited ES2, ES3, or both types of transitions, corresponding to absorbances in the visible from 400 - 700 nm. Furthermore ES3 was the dominant transition for the HE absorbance (λ_{max} ranging from ~400-440 nm). Finally, ES4 was exhibited by six of the different electrochromes. The discussion begins at the lowest significant excited state transition (ES1) and continues for the remaining three most significant states possessing λ_{max} values as low as 400 nm.

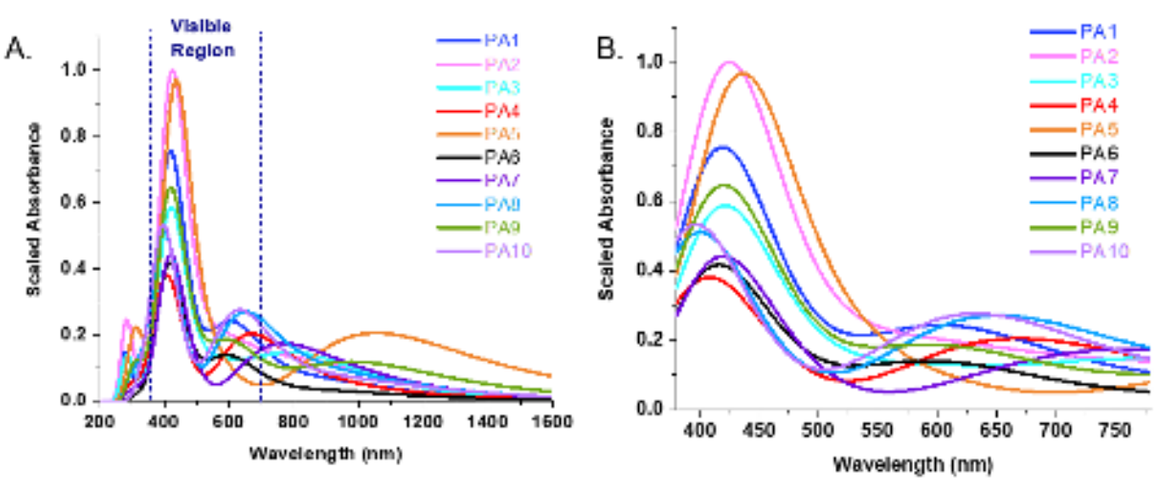

Figure 5. Radical cation UV-Vis spectra for all 10 chromophores where absorbance was normalized by both the largest absorbance as well as the oscillator strength. In **A.)** the entire UV to NIR spectrum is displayed and in **B.)** only the visible range is shown.

Table 3. A detailed list of the radical cation excited states and their corresponding wavelengths, oscillator strengths (*f*) and transitions in which only those states which possessed $f \geq 0.1000$ were chosen.

ACE	ES1			ES2			ES3			ES4		
	λ_{nm}	*f*	transition	λ_{nm}	*f*	transition	λ_{nm}	*f*	transition	λ_{nm}	*f*	transition
PA1	608	0.2095	**S_β–1→L_β**	N/A	N/A	N/A	425	0.5392	**S_α→L_α**	404	0.1434	**S_β–3→L_β** S_β–5→L_β
PA2	N/A	N/A	N/A	559	0.1097	**S_β–2→L_β**	424	0.7139	**S_α→L_α**	N/A	N/A	N/A
PA3	769	0.1016	S_β→L_β **S_β–1→L_β**	569	0.1129	**S_β–2→L_β**	414	0.4192	**S_α→L_α** S_β–3→L_β	437	0.2400	S_α→L_α **S_β–3→L_β**
PA4	N/A	N/A	N/A	661	0.2372	**S_β–2→L_β**	401 430	0.2719 0.1913	**S_α→L_α** S_β–5→L_β **S_α→L_α**	N/A	N/A	N/A
PA5	1056	0.1521	**S_β→L_β**	N/A	N/A	N/A	436	0.6912	**S_α→L_α**	N/A	N/A	N/A
PA6	N/A	N/A	N/A	598	0.2109	**S_β–2→L_β**	431	0.2585	**S_α→L_α**	409	0.2976	S_α→L_α **S_β–3→L_β**
PA7	N/A	N/A	N/A	727	0.1962	**S_β–2→L_β**	N/A	N/A	N/A	416 420	0.2572 0.3151	S_α→L_α **S_β–3→L_β** S_α→L_α **S_β–5→L_β**
PA8	N/A	N/A	N/A	645	0.2229	**S_β–2→L_β**	402	0.3644	**S_α→L_α**	N/A	N/A	N/A
PA9	998	0.1102	**S_β→L_β**	604	0.1675	**S_β–2→L_β**	417	0.4612	**S_α→L_α**	444	0.1449	S_α→L_α **S_β–3→L_β**
PA10	N/A	N/A	N/A	630	0.2288	**S_β–2→L_β**	400	0.3801	**S_α→L_α**	N/A	N/A	N/A

E1. ES1: PA1, PA3, PA5, PA9 ($S_\beta \rightarrow L_\beta$ & S_β-1 $\rightarrow L_\beta$)

The first set of transitions, categorized as ES1, are the result of the S_β or the S_β–1 to L_β excitation which occurred for **PA5**, **PA9**, **PA3** and **PA1**. The molecular orbital diagrams given from longest to shortest wavelength are shown in **Figure 6** and **Figure S4A.** Additionally, all possessed low *f* values (<0.25) causing the resultant peaks to appear wide and flat spectroscopically (**Figure 5B**). Both **PA5** and **PA9** exhibited NIR absorptions resulting from the S_β to L_β transition. Furthermore, there was a 50 nm blue-shift for **PA9** relative to **PA5** likely due to the additional methoxy group and the 4.7° additional twist out of plane. The S_β molecular orbital for **PA5** had electron density on the EDOT sulfur lacking in **PA9** (**Figure 6B** – pink circles), where instead, there is a small amount of electron density on the third methoxy (**Figure 6B** – green circles). Otherwise, the remaining electron density distribution for S_β and all of L_β show a nearly identical pattern for both of these electrochromes. Comparatively, **PA3** indicates a more than 200 nm blue-shift, due to the lack of S-O stabilization that were found in both **PA5** and **PA9** (**Figure 6C**– yellow oval). While the S_β to L_β excitation is partly responsible for the 769 nm absorption, it is the S_β-1 to L_β which is the main contributor to ES1. Finally, the S_β-1 to L_β transition for **PA1** indicates a 150 nm blue-shift relative to PA3 caused by the absence of the electron-donating OCH_3 group (**Figure 6D**– orange circles). These findings are consistent with our previous work

for which increasing electron density promotes the lower energy transition S_β to L_β as observed in **PA5** and **PA9**. In comparison, less electron rich systems like **PA1** (0 methoxy groups) and **PA3** (1 methoxy group) the higher energy transitions S_β-1 to L_β is observed. These transitions are important because they give rise to the position of the lower energy absorbance within the spectral range. Since both **PA1** and **PA3** display transitions occurring in the visible, the shape of the peaks derived from the ES1 transition may influence their radical cation color. Additionally, an examination of the λ_{max} and corresponding *f* values suggest that **PA1** would be a better synthetic target than **PA3**. However, given the 161 nm difference between these wavelengths combining both would help tune the resulting color and as such both could be considered worthy of synthesis. Nonetheless, the possible synthetic order utilizing this data would be **PA1**, **PA3**, **PA9** then **PA5**.

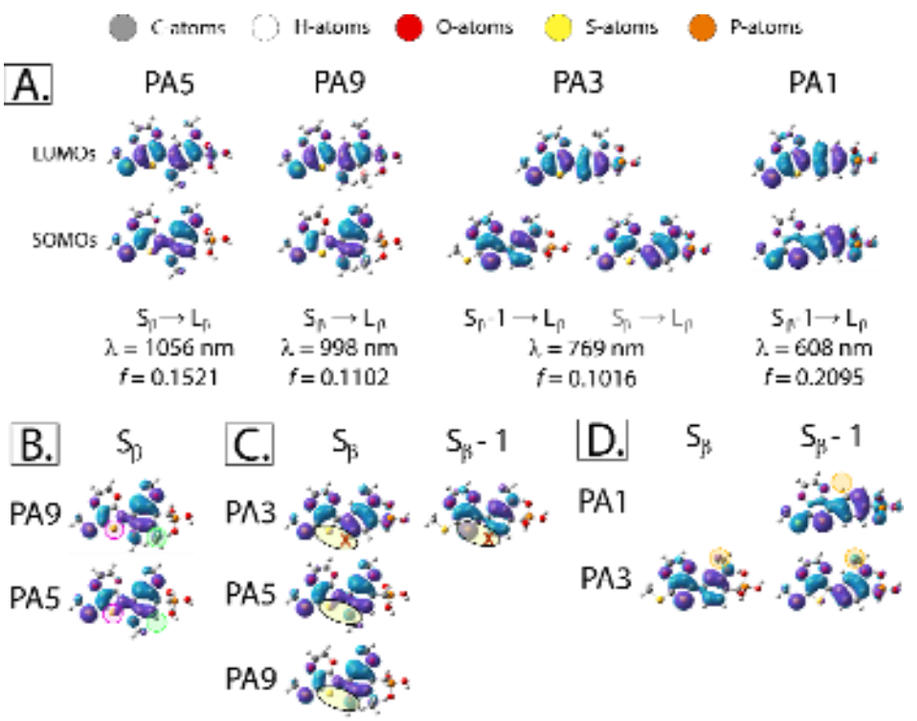

Figure 6. A. All four electrochromes participating in ES1 with transition levels and corresponding wavelengths and oscillator strengths. **B.** $SOMO_\beta$ Comparison of **PA9** & **PA5** **C.** $SOMO_\beta$-$SOMO_\beta$-1 Comparison of **PA9** & **PA5** to **PA3** **D.** $SOMO_\beta$/$SOMO_\beta$-1 Comparison of **PA3** & **PA1**

E2. ES2: PA2, PA3, PA4, PA6, PA7, PA8, PA9, and PA10 (S_β-2 → L_β)

ES2 is exhibited by all chromophores with the exception of **PA1** and **PA5** and was produced by the S_β-2 to L_β transition (**Figure S5**). In **Figure S5A** the molecular orbitals for this set are arranged from longest to shortest wavelengths as well as into groups which express similar electron density arrangements. The **PA7** chromophore had the most red-shifted wavelength (727

nm, *f* = 0.200). The analog of **PA7**, **PA4**, is blue-shifted by 66 nm which is the consequence of the steric interaction between the EDOT and the adjacent methoxy groups thereby causing a more than 30° twist out of plane. Additionally, **PA4** was the only electrochrome which lacked electron density on the PA side of the phenyl ring (**Figure S5B** – pink circle). Both **PA7** and **PA4** have a unique S_β-2 electron density pattern compared to each other and the rest of the series. The **PA8** and **PA10** absorbance are blue-shifted by 17 nm and 31 nm relative to **PA4**. Their electron densities for S_β-2 differ slightly in pattern between the two rings (**Figure S5C** – green rectangle) as well as in the methoxy density on the EDOT side of **PA8** (**Figure S5C** – gray circle). This finding coupled with the 14 nm λ_{max} difference is further evidence that there is minimal impact when an additional methoxy is added on the phosphonic acid side. **PA6** and **PA9** were blue-shifted from **PA8** by 26 nm and 32 nm, respectively. Like **PA8** and **PA10**, going from **PA6** to **PA9** in which a third methoxy was added to the phosphonic side resulted in only a minor shift in electron density on the phenylene (**Figure S5D** – orange circle) and a 6 nm difference. Finally, analogs **PA2** and **PA3** are blue-shifted by 19 nm and 29 nm from **PA6**, respectively, and 10 nm from each other. These two are lack the electron density from the additional methoxys which is present in the other systems which exhibit this transition. Additionally, this set demonstrates that methoxy groups placed on the phosphonic acid side of the phenylene have a much smaller impact than those affixed on the EDOT side. To generate a list of synthesis worthy targets we will use both the oscillator strengths coupled with the λ_{max} values. The *f* values from highest to lowest (with corresponding λ_{max} values) are **PA4** (0.2372, 661 nm), **PA10** (0.2288, 630 nm), **PA8** (0.2229, 644 nm), **PA6** (0.2109, 598 nm), **PA7** (0.1962, 727 nm), **PA9** (0.1675, 604 nm), **PA3** (0.1129, 569 nm), then **PA2** (0.1097, 559nm). Considering both of these values, the suggested synthetic order would be: **PA4**, **PA10**, **PA8**, **PA9**, **PA7**, then **PA3**. As **PA9** is only 6 nm red-shifted relative to **PA6** and **PA2** is 10 nm red-shifted relative to **PA3,** but **PA9** and **PA2** have the higher *f* values, thus neither **PA6** nor **PA3** are worthy of synthesis.

E3. ES3: all but PA7 ($S_\alpha \rightarrow L_\alpha$)

The S_α to L_α transition was responsible for ES3 (see **Figure S6** for the MOs) and produced the spectral λ_{max} for all electrochromes with the exception of **PA6** and **PA7**. Furthermore, **PA7** is not discussed here as the S_α to L_α transition was not observed to be a primary contributor for any of the excited states. For **PA4** and **PA9**, this transition occurred at shorter wavelengths than that of ES4, and as such, the order of states will appear reversed in **Table 3**. **Figure S6** shows the chromophores segmented into three sets based on either the λ_{max} (Group 1: **PA5** > **PA6** > **PA1** ~ **PA2** > **PA9**; Group 2: **PA8** > **P10**) or the presence of an accompanying transition (Group 3: **PA3**

and **PA4**). The geometry and the stabilization trends support the absorption order for Group 1, which ranges from 436 nm to 417 nm. For example, **PA5** is the most planar and possesses only stabilization interactions versus **PA9**, which is the least planar in this set and has two adjacent oxygen atoms separated by only 2.73 Å. Additionally, the only noticeable difference in the SOMOα is the electron density pattern of the C-4 atom in the phenyl ring (**Figure S6B** – pink arrow/circle). Furthermore, there is only 2 nm separating **PA8** and **PA10**, which correlates well to the differences between their stabilization separations (≤ 0.1 Å) and nonplanarity (1.6°). Moreover, there is slightly more electron density on the EDOT S-atom for **PA10** (**Figure S6C**– yellow circle/black arrow) and less on the benzene C-5 carbon (**Figure S6C** – green rectangle/arrow). Finally, Group 3 chromophores also follow these trends where the 13 nm blue-shift exhibited by **PA4** relative to **PA3** is primarily due to the additional 26° twist which is also responsible for the electron density distribution difference (**Figure S6D**). For highest to lowest *f* values (corresponding λ_{max}) we have: **PA2** (0.7139, 424 nm), **PA5** (0.6912, 436 nm), **PA1** (0.5392, 425 nm), **PA9** (0.4612, 417 nm), **PA3** (0.4192, 414 nm), **PA10** (0.3801, 400 nm), **PA8** (0.3644, 402 nm), **PA4** (0.2719, 401 nm), **PA6** (0.2585 598 nm), and **PA4** (0.1913, 430 nm). With these in mind the suggested synthetic order would be: **PA2**, **PA5**, **PA9**, then **PA10**. The remaining electrochromes possess comparable wavelengths to these four with smaller oscillator strengths and therefore would not be considered.

E4. ES4: PA1, PA3, PA4, PA6, PA7, and PA9 (S_{β}-3 → L_{β} & S_{β}-5 → L_{β})

The ES4 electronic transitions are contributed by $S_{\beta\text{-}3}$ to L_{β} and/or $S_{\beta\text{-}5}$ to L_{β} which we will treat individually (see **Figure S7A** for MO diagrams). For the set generated from the $S_{\beta\text{-}3}$ to L_{β} transition, the absorptions ranged from 437 nm to 404 nm. **Figure S7B** shows the diagrams arranged by similarities in the distribution pattern. In the case of **PA9** and **PA6** the only noticeable deviation is the increased density on the *cis*-methoxy substituents for **PA6** (**Figure S7B**– pink oval). **PA1** and **PA3** have similar densities on the two S-atoms (**Figure S7B** – green rectangle) but differ for the remainder of the system. On the other hand, **PA3** has an indistinguishable electron density on the phosphonic acid-substituent compared to **PA7** (**Figure S7B** –black circle). Finally, only **PA7** possessed the $S_{\beta\text{-}5}$ to L_{β} transition as the primary contributor to ES4 which was also responsible for the λ_{max} (**Table 3**).

Utilizing the molecular orbital analysis, we are afforded a more insightful understanding of the relationship between UV-Vis simulated spectra and the radical cation molecular orbitals from which the transitions therein are produced. In particular, we have monitored the influence of structural modifications of these orbitals which lead to the spectra and eventually the color. For our radical cation excited state analysis (see **Table S5**), we ranked all the wavelengths of

absorption from longest to shortest. Additionally, we eliminated chromophores which possessed λ_{max} that differed from another by less than 10 nm while exhibiting a smaller oscillator strength (i.e. **PA5** (0.6912, 436 nm) vs **PA3** (0.2400, 437 nm) vs **PA9** (0.1449, 444 nm). From this treatment, **PA1**, and **PA8** were discarded as possible synthetic targets. The remaining electrochromes in order from most to least promising are: **PA2**, **PA5**, **PA9**, **PA10**, **PA4**, **PA6**, **PA7** and **PA3**.

F. Selection of PAX Chromophores for Future Synthesis

Finally, we utilize the geometric results from both the neutral and radical cation forms as well as the radical cation excited state transition analysis (see **Table S6**) in order to identify the most promising chromophores for use in electrochromic devices. Applying the results for all three studies, our recommended order of synthetic targets is: **PA5**, **PA2**, **PA9**, **PA6**, **PA7**, **PA4**, **PA3**, and **PA10**. We continue to consider **PA5** in spite of the visible tailing into the neutral as this effect is minor and may be reduced under experimental conditions. Additionally, should **PA9** be too synthetically challenging we would suggest generating **PA6** after **PA2** then **PA7**, etc.

G. Conclusion & Perspective:

In summary, a thiol hexyl ether functionalized EDOT conjugated to a *para*-phenyl phosphonic acid, **PA1**, and its phosphonate derivative, **PA1E**, were synthesized as a preliminary proof-of-concept of an ACE molecule capable of adsorbing onto a metal oxide surface. Theory provided insight into the geometries and excited states for the neutral and oxidized set of electrochromes. There were nearly identical geometries, FMOs, and excited state transitions for both **PA1** and **PA1E**. Calculations and experimental absorbance spectra demonstrate that **PA1E** in solution overlaps with **PA1** adsorbed onto nano-ITO, indicating that these chromophores exhibit the same optical properties; hence the calculations provided accurate spectral predictions. Also, **PA1** oxidizes at 0.96 V vs. Ag/AgCl, which is within the oxidation potential window (0.80 V to 1.2 V) of the anodically coloring electrochromes examined by Ntera LTD.[68]

Motivated by these results, we investigated a new family of chromophores that expanded on **PA1**'s structural scaffold to understand how steric interactions, electronics, and geometry affect the radical cation absorbance position and intensity. Nine additional bi-aryl EDOT-X-Phenyl-Phosphonic Acid chromophores possessing various methoxy groups, **PA2**-**PA10**, were investigated using TD-DFT. With the exception of **PA5**, all neutral state absorbances fell within the UV region and are therefore predicted to be fully transmissive. Analysis of dihedral angles and atomic distances revealed that methoxy groups placed on the same side as EDOT generated

more significant geometric and electronic stabilization effects than when placed on the phosphonic acid side. Both O-S and O-H interactions aided in planarizing the radical cation species, whereas methoxy groups placed *ortho* to each other induced O-O repulsion as well as an increase in torsional strain. Furthermore, four different excited state transitions (near the visible range) were observed across the set. In the radical cation absorbance spectra, the S_α to L_α transition accounted for the narrow higher energy peak ranging between 400-430 nm, and the $S_\beta \rightarrow L_\beta$, S_β-1 $t \rightarrow L_\beta$, and S_β-2 $\rightarrow L_\beta$ transitions contributed to the broad lower energy peak located between 560-1050 nm. Steric interactions also influenced the radical cation λ_{max} position, for which O-S stabilization aided in red-shifting the higher energy absorbance peak position. According to their optical and geometric properties, we propose that **PA2** and **PA5** be prioritized for future synthetic efforts. Functionalizing **PA5** with bulky alkylated methoxy substituents may blue-shift its neutral absorbance into the UV region, thus overcoming the possible tailing into the visible. **PA9** is also a possible target, however this sterically hindered trimethoxy phenyl core may pose some synthetic challenges and as such **PA6** may be our third synthetic target.

Currently, calculations have provided accurate predictions for the higher energy absorbance peaks that demonstrate strong agreement with experimental observations; however, the calculated lower energy peaks often appear broad and flat. In these bi-aryl ring systems, color and saturation control often rely on this second band; thus, color prediction remains a challenge. In the future, the structure-property relationship between chromophores and the shape of the radical cation lower energy peak will be further investigated as new ACEs are developed.

Supplementary Material: a separate document which includes all coordinates, molecular orbital levels, experimental characterization, molecular orbital diagrams and overall analyses to identify synthetic target order

Acknowledgments
Funding from the Air Force Office of Scientific Research (FA9550-18-1-0184 and FA9550-18-1-0034) and supercomputer access through the National Science Foundation's Extreme Science and Engineering Discovery Environment (NSF XSEDE, DMR 160146).

Conflict of Interest
The authors declare the following competing financial interest(s): Electrochromic polymer technology developed at the Georgia Institute of Technology has been licensed to NXN Licensing. JRR serves as consultants to NXN Licensing.

Data Availability
The data that supports the findings in this study are available within the article [and its supplementary material].

References:

(1) Gillaspie, D. T.; Tenent, R. C.; Dillon, A. C. Metal-Oxide Films for Electrochromic Applications: Present Technology and Future Directions. *J. Mater. Chem.* **2010**, *20* (43), 9585.

(2) Zhai, Y.; Li, Y.; Zhang, H.; Yu, D.; Zhu, Z.; Sun, J.; Dong, S. Self-Rechargeable-Battery-Driven Device for Simultaneous Electrochromic Windows, ROS Biosensing, and Energy Storage. *ACS Appl. Mater. Interfaces* **2019**, *11* (31), 28072–28077.

(3) Vega-Colado, C.; Vergaz Benito, R.; Sanchez-Pena, J. M.; Alesanco, Y.; Vinuales, A.; Cuadrado-Asensio, R. Driving Signals Optimization for Viologen-Based Electrochromic Vision Devices. *IEEE Sens. J.* **2019**, *19* (5), 1740–1747.

(4) Wang, C.; Wang, Z.; Ren, Y.; Hou, X.; Yan, F. Flexible Electrochromic Zn Mirrors Based on Zn/Viologen Hybrid Batteries. *ACS Sustain. Chem. Eng.* **2020**, *8* (13), 5050–5055.

(5) Zhai, Y.; Li, Y.; Zhu, Z.; Zhu, C.; Du, D.; Lin, Y. Self-Driven Multicolor Electrochromic Energy Storage Windows Powered by a "Perpetual" Rechargeable Battery. *ACS Appl. Mater. Interfaces* **2019**, *11* (51), 48013–48020.

(6) Ke, Y.; Chen, J.; Lin, G.; Wang, S.; Zhou, Y.; Yin, J.; Lee, P. S.; Long, Y. Smart Windows: Electro-, Thermo-, Mechano-, Photochromics, and Beyond. *Adv. Energy Mater.* **2019**, *9* (39), 1902066.

(7) Xia, X.; Ku, Z.; Zhou, D.; Zhong, Y.; Zhang, Y.; Wang, Y.; Huang, M. J.; Tu, J.; Fan, H. J. Perovskite Solar Cell Powered Electrochromic Batteries for Smart Windows. *Mater. Horizons* **2016**, *3* (6), 588–595.

(8) Li, H.; McRae, L.; Firby, C. J.; Elezzabi, A. Y. Rechargeable Aqueous Electrochromic Batteries Utilizing Ti-Substituted Tungsten Molybdenum Oxide Based Zn 2+ Ion Intercalation Cathodes. *Adv. Mater.* **2019**, *31* (15), 1807065.

(9) Chen, J.; Wang, Z.; Chen, Z.; Cong, S.; Zhao, Z. Fabry–Perot Cavity-Type Electrochromic Supercapacitors with Exceptionally Versatile Color Tunability. *Nano Lett.* **2020**, *20* (3), 1915–1922.

(10) Cao, S.; Zhang, S.; Zhang, T.; Yao, Q.; Lee, J. Y. A Visible Light-Near-Infrared Dual-Band Smart Window with Internal Energy Storage. *Joule* **2019**, *3* (4), 1152–1162.

(11) Celiesiute, R.; Ramanaviciene, A.; Gicevicius, M.; Ramanavicius, A. Electrochromic Sensors Based on Conducting Polymers, Metal Oxides, and Coordination Complexes. *Crit. Rev. Anal. Chem.* **2019**, *49* (3), 195–208.

(12) Ranjbar, S.; Nejad, M. A. F.; Parolo, C.; Shahrokhian, S.; Merkoçi, A. Smart Chip for Visual Detection of Bacteria Using the Electrochromic Properties of Polyaniline. *Anal.*

Chem. **2019**, *91* (23), 14960–14966.

(13) Mortimer, R. J.; Dyer, A. L.; Reynolds, J. R. Electrochromic Organic and Polymeric Materials for Display Applications. *Displays* **2006**, *27* (1), 2–18.

(14) Bae, S.; Kim, H.; Lee, Y.; Xu, X.; Park, J.-S.; Zheng, Y.; Balakrishnan, J.; Lei, T.; Ri Kim, H.; Song, Y. Il; Kim, Y.-J.; Kim, K. S.; Özyilmaz, B.; Ahn, J.-H.; Hong, B. H.; Iijima, S. Roll-to-Roll Production of 30-Inch Graphene Films for Transparent Electrodes. *Nat. Nanotechnol.* **2010**, *5* (8), 574–578.

(15) Xiong, J.; Lin, M.-F.; Wang, J.; Gaw, S. L.; Parida, K.; Lee, P. S. Wearable All-Fabric-Based Triboelectric Generator for Water Energy Harvesting. *Adv. Energy Mater.* **2017**, *7* (21), 1701243.

(16) Yeh, M.; Lin, L.; Yang, P.; Wang, Z. L.; States, U. Motion-Driven Electrochromic Smart Window System. *ACS Nano* **2015**, *9* (5), 4757–4765.

(17) Amb, C. M.; Kerszulis, J. A.; Thompson, E. J.; Dyer, A. L.; Reynolds, J. R. Propylenedioxythiophene (ProDOT)–Phenylene Copolymers Allow a Yellow-to-Transmissive Electrochrome. *Polym. Chem.* **2011**, *2* (4), 812.

(18) Sonmez, G.; Sonmez, H. B.; Shen, C. K. F.; Wudl, F. Red, Green, and Blue Colors in Polymeric Electrochromics. *Adv. Mater.* **2004**, *16* (21), 1905–1908.

(19) Sheng, K.; Xu, F.; Shen, K.; Zheng, J.; Xu, C. Electrocatalytic PProDOT–Me2 Counter Electrode for a Br−/Br3− Redox Couple in a WO3-Based Electrochromic Device. *Electrochem. commun.* **2020**, *111* (December 2019), 106646.

(20) Dautremont-Smith, W. C. Transition Metal Oxide Electrochromic Materials and Displays: A Review. *Displays* **1982**, *3* (2), 67–80.

(21) Zhou, D.; Xie, D.; Xia, X.; Wang, X.; Gu, C.; Tu, J. All-Solid-State Electrochromic Devices Based on WO3||NiO Films: Material Developments and Future Applications. *Sci. China Chem.* **2017**, *60* (1), 3–12.

(22) Xia, X. H.; Tu, J. P.; Zhang, J.; Xiang, J. Y.; Wang, X. L.; Zhao, X. B. Cobalt Oxide Ordered Bowl-Like Array Films Prepared by Electrodeposition through Monolayer Polystyrene Sphere Template and Electrochromic Properties. *ACS Appl. Mater. Interfaces* **2010**, *2* (1), 186–192.

(23) Xia, X. H.; Tu, J. P.; Zhang, J.; Huang, X. H.; Wang, X. L.; Zhang, W. K.; Huang, H. Enhanced Electrochromics of Nanoporous Cobalt Oxide Thin Film Prepared by a Facile Chemical Bath Deposition. *Electrochem. commun.* **2008**, *10* (11), 1815–1818.

(24) Schwendeman, I.; Hickman, R.; Sönmez, G.; Schottland, P.; Zong, K.; Welsh, D. M.; Reynolds, J. R. Enhanced Contrast Dual Polymer Electrochromic Devices. *Chem. Mater.*

2002, *14* (7), 3118–3122.

(25) Wu, W.; Wang, M.; Ma, J.; Cao, Y.; Deng, Y. Electrochromic Metal Oxides: Recent Progress and Prospect. *Adv. Electron. Mater.* **2018**, *4* (8), 1800185.

(26) Granqvist, C. G. Oxide Electrochromics: An Introduction to Devices and Materials. *Sol. Energy Mater. Sol. Cells* **2012**, *99*, 1–13.

(27) Devan, R. S.; Patil, R. A.; Lin, J.-H.; Ma, Y.-R. One-Dimensional Metal-Oxide Nanostructures: Recent Developments in Synthesis, Characterization, and Applications. *Adv. Funct. Mater.* **2012**, *22* (16), 3326–3370.

(28) Dyer, A. L.; Thompson, E. J.; Reynolds, J. R. Completing the Color Palette with Spray-Processable Polymer Electrochromics. *ACS Appl. Mater. Interfaces* **2011**, *3* (6), 1787–1795.

(29) Beaujuge, P. M.; Reynolds, J. R. Color Control in π-Conjugated Organic Polymers for Use in Electrochromic Devices. *Chem. Rev.* **2010**, *110* (1), 268–320.

(30) Han, Y.; Xing, Z.; Ma, P.; Li, S.; Wang, C.; Jiang, Z.; Chen, Z. Design Rules for Improving the Cycling Stability of High-Performance Donor–Acceptor-Type Electrochromic Polymers. *ACS Appl. Mater. Interfaces* **2020**, *12* (6), 7529–7538.

(31) Han, F. S.; Higuchi, M.; Kurth, D. G. Metallosupramolecular Polyelectrolytes Self-Assembled from Various Pyridine Ring-Substituted Bisterpyridines and Metal Ions: Photophysical, Electrochemical, and Electrochromic Properties. *J. Am. Chem. Soc.* **2008**, *130* (6), 2073–2081.

(32) Sun, Y.; Shi, M.; Zhu, Y.; Perepichka, I. F.; Xing, X.; Liu, Y.; Yan, C.; Meng, H. Multicolored Cathodically Coloring Electrochromism and Electrofluorochromism in Regioisomeric Star-Shaped Carbazole Dibenzofurans. *ACS Appl. Mater. Interfaces* **2020**, *12* (21), 24156–24164.

(33) Argazzi, R.; Murakami Iha, N. Y.; Zabri, H.; Odobel, F.; Bignozzi, C. A. Design of Molecular Dyes for Application in Photoelectrochemical and Electrochromic Devices Based on Nanocrystalline Metal Oxide Semiconductors. *Coord. Chem. Rev.* **2004**, *248* (13–14), 1299–1316.

(34) Wang, M.; Fan, J.; Lu, H.; Huang, M.; Qiao, X.; Yang, J. Multiarm Aniline Oligomers: Molecular Architecture, Self-Assembly, and Electrochromic Performance. *J. Phys. Chem. C* **2020**, *124* (14), 7844–7852.

(35) Buch, V. R.; Chawla, A. K.; Rawal, S. K. Review on Electrochromic Property for WO3 Thin Films Using Different Deposition Techniques. *Mater. Today Proc.* **2016**, *3* (6), 1429–1437.

(36) Shi, Y.; Sun, M.; Zhang, Y.; Cui, J.; Shu, X.; Wang, Y.; Qin, Y.; Liu, J.; Tan, H. H.; Wu, Y. Rational Design of Oxygen Deficiency-Controlled Tungsten Oxide Electrochromic Films with an Exceptional Memory Effect. *ACS Appl. Mater. Interfaces* **2020**, *12* (29), 32658–32665.

(37) Rong, K.; Zhang, H.; Zhang, H.; Hu, Y.-Y.; Fang, Y.; Dong, S. Deep Eutectic Solvent with Prussian Blue and Tungsten Oxide for Green and Low-Cost Electrochromic Devices. *ACS Appl. Electron. Mater.* **2019**, *1* (6), 1038–1045.

(38) Cai, G.; Cui, M.; Kumar, V.; Darmawan, P.; Wang, J.; Wang, X.; Lee-Sie Eh, A.; Qian, K.; Lee, P. S. Ultra-Large Optical Modulation of Electrochromic Porous WO 3 Film and the Local Monitoring of Redox Activity. *Chem. Sci.* **2016**, *7* (2), 1373–1382.

(39) Li, G.; Song, R.; Ma, W.; Liu, X.; Li, Y.; Rao, B.; He, G. π-Extended Chalcogenoviologens with Stable Radical State Enable Enhanced Visible-Light-Driven Hydrogen Evolution and Static/Dynamic Electrochromic Displays. *J. Mater. Chem. A* **2020**, *8* (25), 12278–12284.

(40) Kim, M.; Kim, Y. M.; Moon, H. C. Asymmetric Molecular Modification of Viologens for Highly Stable Electrochromic Devices. *RSC Adv.* **2019**, *10* (1), 394–401.

(41) Shi, Y.; Wang, G.; Chen, Q.; Zheng, J.; Xu, C. Electrochromism and Electrochromic Devices of New Extended Viologen Derivatives with Various Substituent Benzene. *Sol. Energy Mater. Sol. Cells* **2020**, *208*, 110413.

(42) Beaujuge, P. M.; Reynolds, J. R. Color Control in π-Conjugated Organic Polymers for Use in Electrochromic Devices. *Chem. Rev.* **2010**, *110* (1), 268–320.

(43) Kerszulis, J. A.; Bulloch, R. H.; Teran, N. B.; Wolfe, R. M. W.; Reynolds, J. R. Relax: A Sterically Relaxed Donor-Acceptor Approach for Color Tuning in Broadly Absorbing, High Contrast Electrochromic Polymers. *Macromolecules* **2016**, *49* (17), 6350–6359.

(44) Christiansen, D. T.; Reynolds, J. R. A Fruitful Usage of a Dialkylthiophene Comonomer for Redox Stable Wide-Gap Cathodically Coloring Electrochromic Polymers. *Macromolecules* **2018**, *51* (22), 9250–9258.

(45) Shin, H.; Kim, Y.; Bhuvana, T.; Lee, J.; Yang, X.; Park, C.; Kim, E. Color Combination of Conductive Polymers for Black Electrochromism. *ACS Appl. Mater. Interfaces* **2012**, *4* (1), 185–191.

(46) Cao, K.; Shen, D. E.; Österholm, A. M.; Kerszulis, J. A.; Reynolds, J. R. Tuning Color, Contrast, and Redox Stability in High Gap Cathodically Coloring Electrochromic Polymers. *Macromolecules* **2016**, *49* (22), 8498–8507.

(47) Schwendeman, I.; Gaupp, C. L.; Hancock, J. M.; Groenendaal, L.; Reynolds, J. R. Perfluoroalkanoate-Substituted PEDOT for Electrochromic Device Applications. *Adv.*

Funct. Mater. **2003**, *13* (7), 541–547.

(48) Christiansen, D. T.; Tomlinson, A. L.; Reynolds, J. R. New Design Paradigm for Color Control in Anodically Coloring Electrochromic Molecules. *J. Am. Chem. Soc.* **2019**, *141* (9), 3859–3862.

(49) Devan, R. S.; Gao, S.-Y.; Ho, W.-D.; Lin, J.-H.; Ma, Y.-R.; Patil, P. S.; Liou, Y. Electrochromic Properties of Large-Area and High-Density Arrays of Transparent One-Dimensional β-Ta2O5 Nanorods on Indium-Tin-Oxide Thin-Films. *Appl. Phys. Lett.* **2011**, *98* (13), 133117.

(50) Jiang, S.; Yuan, G.; Hua, C.; Khan, S.; Wu, Z.; Liu, Y.; Wang, J.; Song, C.; Han, G. Electrochromic Properties of Ni/NiO/RGO Nanocomposite Films Prepared by a Facile Sol-Gel Technique. *J. Electrochem. Soc.* **2017**, *164* (13), H896–H902.

(51) Cai, G.; Tu, J.; Zhang, J.; Mai, Y.; Lu, Y.; Gu, C.; Wang, X. An Efficient Route to a Porous NiO/Reduced Graphene Oxide Hybrid Film with Highly Improved Electrochromic Properties. *Nanoscale* **2012**, *4* (18), 5724.

(52) Ellinger, S.; Graham, K. R.; Shi, P.; Farley, R. T.; Steckler, T. T.; Brookins, R. N.; Taranekar, P.; Mei, J.; Padilha, L. A.; Ensley, T. R.; Hu, H.; Webster, S.; Hagan, D. J.; Van Stryland, E. W.; Schanze, K. S.; Reynolds, J. R. Donor–Acceptor–Donor-Based π-Conjugated Oligomers for Nonlinear Optics and Near-IR Emission. *Chem. Mater.* **2011**, *23* (17), 3805–3817.

(53) Parker, T. C.; Patel, D. G. (Dan); Moudgil, K.; Barlow, S.; Risko, C.; Brédas, J.-L.; Reynolds, J. R.; Marder, S. R. Heteroannulated Acceptors Based on Benzothiadiazole. *Mater. Horizons* **2015**, *2* (1), 22–36.

(54) Patel, D. G.; Feng, F.; Ohnishi, Y. Y.; Abboud, K. A.; Hirata, S.; Schanze, K. S.; Reynolds, J. R. It Takes More than an Imine: The Role of the Central Atom on the Electron-Accepting Ability of Benzotriazole and Benzothiadiazole Oligomers. *J. Am. Chem. Soc.* **2012**, *134* (5), 2599–2612.

(55) Lv, X.; Zha, L.; Qian, L.; Xu, X.; Bi, Q.; Xu, Z.; Wright, D. S.; Zhang, C. Controllable Fabrication of Perylene Bisimide Self-Assembled Film and Patterned All-Solid-State Electrochromic Device. *Chem. Eng. J.* **2020**, *386* (December 2019), 123939.

(56) Kortz, C.; Hein, A.; Ciobanu, M.; Walder, L.; Oesterschulze, E. Complementary Hybrid Electrodes for High Contrast Electrochromic Devices with Fast Response. *Nat. Commun.* **2019**, *10* (1), 4874.

(57) Wee, K.-R.; Brennaman, M. K.; Alibabaei, L.; Farnum, B. H.; Sherman, B.; Lapides, A. M.; Meyer, T. J. Stabilization of Ruthenium(II) Polypyridyl Chromophores on Nanoparticle

Metal-Oxide Electrodes in Water by Hydrophobic PMMA Overlayers. *J. Am. Chem. Soc.* **2014**, *136* (39), 13514–13517.

(58) Grätzel, M. Ultrafast Colour Displays. *Nature* **2001**, *409* (6820), 575–576.

(59) Allan, J. T. S.; Quaranta, S.; Ebralidze, I. I.; Egan, J. G.; Poisson, J.; Laschuk, N. O.; Gaspari, F.; Easton, E. B.; Zenkina, O. V. Terpyridine-Based Monolayer Electrochromic Materials. *ACS Appl. Mater. Interfaces* **2017**, *9* (46), 40438–40445.

(60) Lim, B.; Han, S.-Y.; Jung, S.-H.; Jung, Y. J.; Park, J. M.; Lee, W.; Shim, H.-S.; Nah, Y.-C. Synthesis and Electrochromic Properties of a Carbazole and Diketopyrrolopyrrole-Based Small Molecule Semiconductor. *J. Ind. Eng. Chem.* **2019**, *80*, 93–97.

(61) Sampaio, R. N.; Troian-Gautier, L.; Meyer, G. J. A Charge-Separated State That Lives for Almost a Second at a Conductive Metal Oxide Interface. *Angew. Chemie Int. Ed.* **2018**, *57* (47), 15390–15394.

(62) Farnum, B. H.; Wee, K.-R.; Meyer, T. J. Self-Assembled Molecular p/n Junctions for Applications in Dye-Sensitized Solar Energy Conversion. *Nat. Chem.* **2016**, *8* (9), 845–852.

(63) Michaux, K. E.; Gambardella, A. A.; Alibabaei, L.; Ashford, D. L.; Sherman, B. D.; Binstead, R. A.; Meyer, T. J.; Murray, R. W. Visible Photoelectrochemical Water Splitting Based on a Ru(II) Polypyridyl Chromophore and Iridium Oxide Nanoparticle Catalyst. *J. Phys. Chem. C* **2015**, *119* (29), 17023–17027.

(64) Han, H.; Mayer, J. W.; Alford, T. L. Band Gap Shift in the Indium-Tin-Oxide Films on Polyethylene Napthalate after Thermal Annealing in Air. *J. Appl. Phys.* **2006**, *100* (8), 083715.

(65) Hoertz, P. G.; Chen, Z.; Kent, C. A.; Meyer, T. J. Application of High Surface Area Tin-Doped Indium Oxide Nanoparticle Films as Transparent Conducting Electrodes. *Inorg. Chem.* **2010**, *49* (18), 8179–8181.

(66) Sun, X. W.; Wang, J. X. Fast Switching Electrochromic Display Using a Viologen-Modified ZnO Nanowire Array Electrode. *Nano Lett.* **2008**, *8* (7), 1884–1889.

(67) Ganapati, P. Ntera Prints a Display on Almost Any Surface. *Wired*. April 2010, pp 395–410.

(68) Copeland, Gavin ; Briancon, Alain; Moeller, Martin; Leyland, Nigel; Giacoponello, Chris; Cassidy, Micheal; Grave, Christian; Corr, David; Bevk, David; Ryan, M. Advanced Electrode Structures and Electrochromic Devices. US 8,786,932 B2, 2012.

(69) Körzdörfer, T.; Brédas, J.-L. Organic Electronic Materials: Recent Advances in the DFT Description of the Ground and Excited States Using Tuned Range-Separated Hybrid

Functionals. *Acc. Chem. Res.* **2014**, *47* (11), 3284–3291.

(70) Daswani, U.; Singh, U.; Sharma, P.; Kumar, A. From Molecules to Devices: A DFT/TD-DFT Study of Dipole Moment and Internal Reorganization Energies in Optoelectronically Active Aryl Azo Chromophores. *J. Phys. Chem. C* **2018**, *122* (26), 14390–14401.

(71) Sullivan, P. A.; Dalton, L. R. Theory-Inspired Development of Organic Electro-Optic Materials. *Acc. Chem. Res.* **2010**, *43* (1), 10–18.

(72) Zhang, L.; Shen, W.; He, R.; Tang, X.; Yang, Y.; Li, M. Density Functional Study on the Effect of Aromatic Rings Flanked by Bithiophene of Novel Electron Donors in Small-Molecule Organic Solar Cells. *Mater. Chem. Phys.* **2016**, *175*, 13–21.

(73) Sen, A.; Groβ, A. Effect of Electron-Withdrawing/-Donating Groups on the Sensitizing Action of the Novel Organic Dye "3-(5-(4-(Diphenylamino)Styryl)Thiophen-2-Yl)-2-Cyanoacrylic Acid" for N-Type Dye-Sensitized Solar Cells: A Theoretical Study. *J. Phys. Chem. C* **2020**, *124* (16), 8526–8540.

(74) Zhang, J.; Li, H.-B.; Sun, S.-L.; Geng, Y.; Wu, Y.; Su, Z.-M. Density Functional Theory Characterization and Design of High-Performance Diarylamine-Fluorenedyes with Different π Spacers for Dye-Sensitized Solar Cells. *J. Mater. Chem.* **2012**, *22* (2), 568–576.

(75) Barati-darband, F.; Izadyar, M.; Arkan, F. Anchoring Group and π-Spacer Effects on the Dynamics and Kinetics of the Photovoltaic Processes in the Quinoxaline-Based Organic Dye-Sensitized Solar Cells. *J. Phys. Chem. C* **2018**, *122* (42), 23968–23977.

(76) Xu, X.; Zheng, S. Designing New Donor Materials Based on Functionalized DCCnT with Different Electron-donating Groups: A Density Functional Theory (DFT) and Time Dependent Density Functional Theory (TDDFT)-based Study. *Int. J. Quantum Chem.* **2020**, *120* (8), 1–12.

(77) Borges, I.; Uhl, E.; Modesto-Costa, L.; Aquino, A. J. A.; Lischka, H. Insight into the Excited State Electronic and Structural Properties of the Organic Photovoltaic Donor Polymer Poly(Thieno[3,4- b]Thiophene Benzodithiophene) by Means of Ab Initio and Density Functional Theory. *J. Phys. Chem. C* **2016**, *120* (38), 21818–21826.

(78) Manzhos, S.; Pal, A.; Chen, Y.; Giorgi, G. Effect of Organic Cation States on Electronic Properties of Mixed Organic–Inorganic Halide Perovskite Clusters. *Phys. Chem. Chem. Phys.* **2019**, *21* (15), 8161–8169.

(79) Wheeler, D. L.; Rainwater, L. E.; Green, A. R.; Tomlinson, A. L. Modeling Electrochromic Poly-Dioxythiophene-Containing Materials through TDDFT. *Phys. Chem. Chem. Phys.* **2017**, *19* (30), 20251–20258.

(80) Christiansen, D. T.; Ohtani, S.; Chujo, Y.; Tomlinson, A. L.; Reynolds, J. R. All Donor Electrochromic Polymers Tunable across the Visible Spectrum via Random Copolymerization. *Chem. Mater.* **2019**, *31* (17), 6841–6849.

(81) Maroulis, G. Evaluating the Performance of DFT Methods in Electric Property Calculations: Sodium Chloride as a Test Case. *Reports Theor. Chem.* **2013**, 1.

(82) Nabavi, S. H.; Khodabandeh, M. H.; Golbabaee, M.; Moshaii, A. Absorption of DCM Dye in Ethanol: Experimental and Time Dependent Density Functional Study. *Int. J. Opt. Photonics* **2018**, *12* (1), 43–56.

(83) Christiansen, D. T.; Wheeler, D. L.; Tomlinson, A. L.; Reynolds, J. R. Electrochromism of Alkylene-Linked Discrete Chromophore Polymers with Broad Radical Cation Light Absorption. *Polym. Chem.* **2018**, *9* (22), 3055–3066.

(84) Jackson, N. E.; Savoie, B. M.; Kohlstedt, K. L.; Olvera De La Cruz, M.; Schatz, G. C.; Chen, L. X.; Ratner, M. A. Controlling Conformations of Conjugated Polymers and Small Molecules: The Role of Nonbonding Interactions. *J. Am. Chem. Soc.* **2013**, *135* (28), 10475–10483.

(85) Cordero, B.; Gómez, V.; Platero-Prats, A. E.; Revés, M.; Echeverría, J.; Cremades, E.; Barragán, F.; Alvarez, S. Covalent Radii Revisited. *Dalt. Trans.* **2008**, No. 21, 2832.

(86) Li, X.; Perera, K.; He, J.; Gumyusenge, A.; Mei, J. Solution-Processable Electrochromic Materials and Devices: Roadblocks and Strategies towards Large-Scale Applications. *J. Mater. Chem. C* **2019**, *7* (41), 12761–12789.

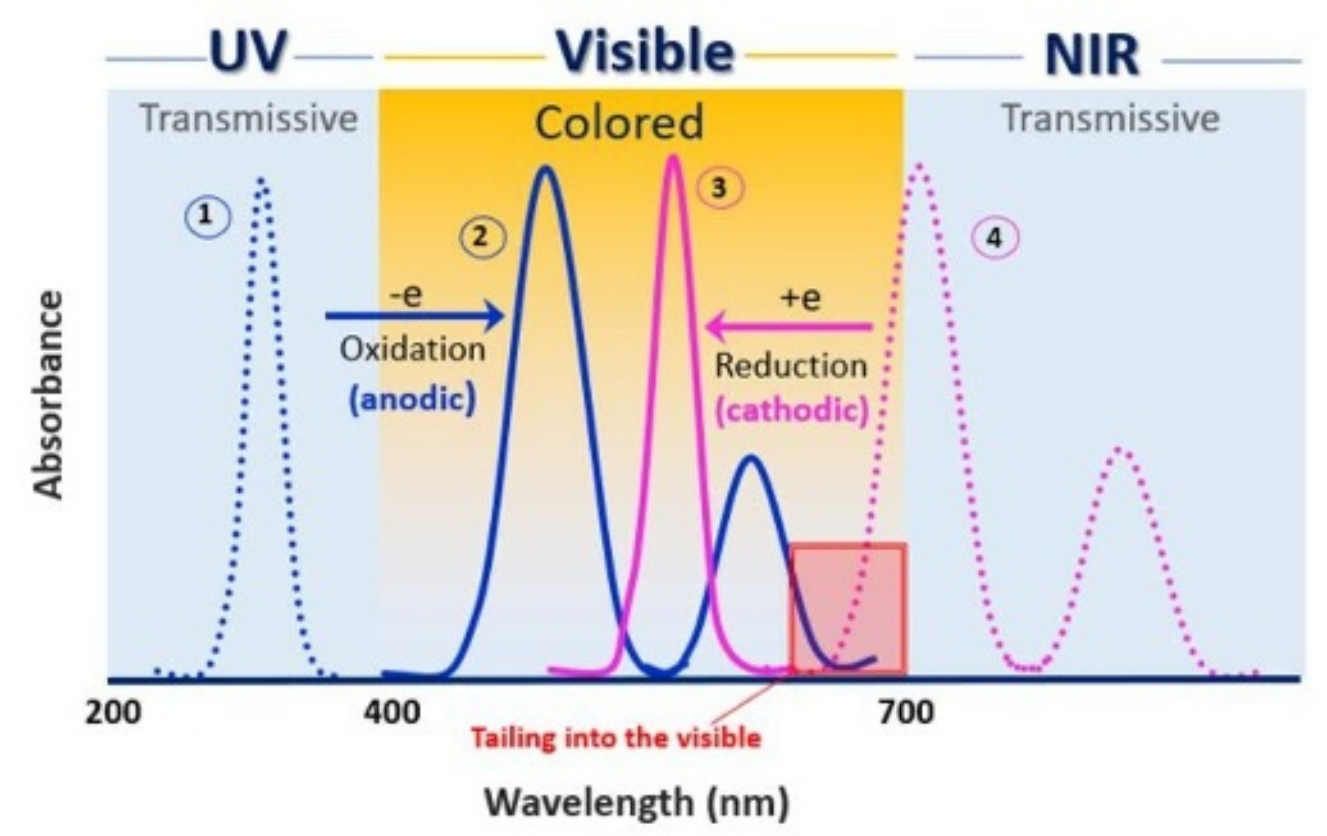
UV
Visible
NIR
Transmissive
Colored
Transmissive
1
2
3
4
-e
Oxidation
(anodic)
+e
Reduction
(cathodic)
Absorbance
200
400
700
Tailing into the visible
Wavelength (nm)

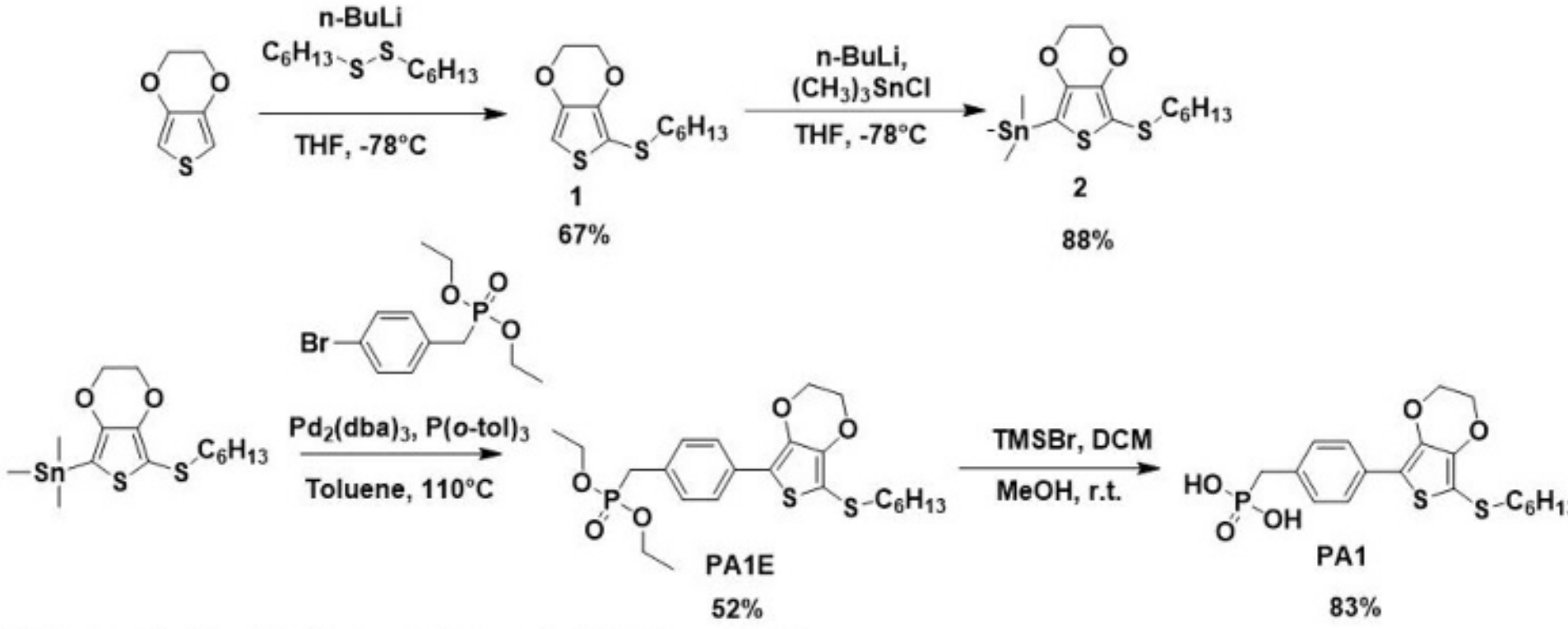

Scheme 1. Synthetic route towards **PA1E** and **PA1**.

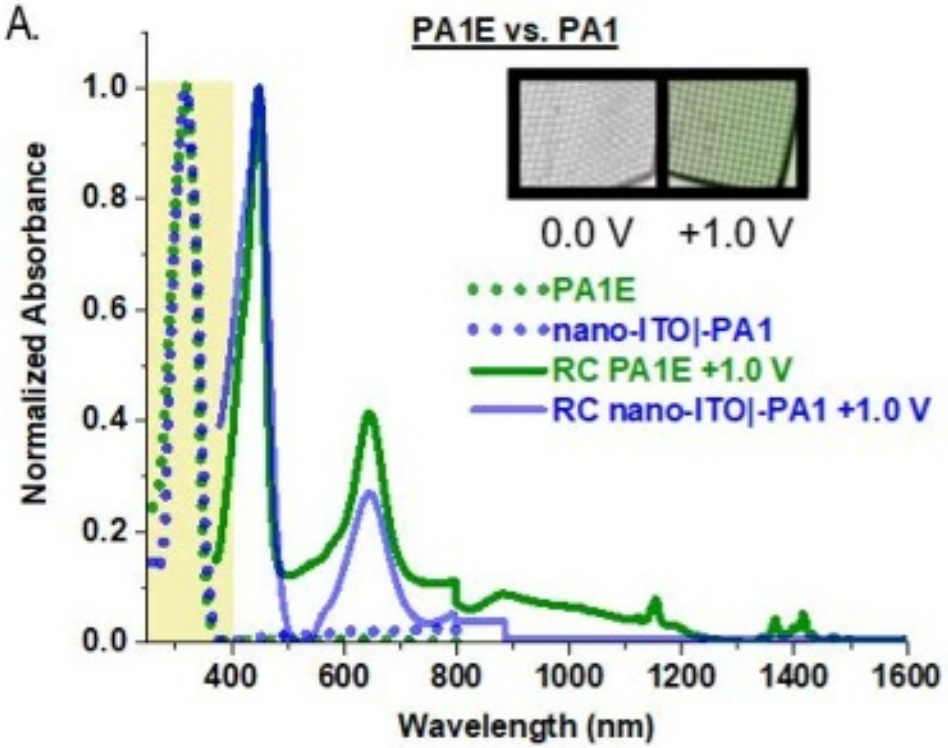
A.
PA1E vs. PA1
0.0 V
+1.0 V
PA1E
nano-ITO|-PA1
RC PA1E +1.0 V
RC nano-ITO|-PA1 +1.0 V
Normalized Absorbance
Wavelength (nm)

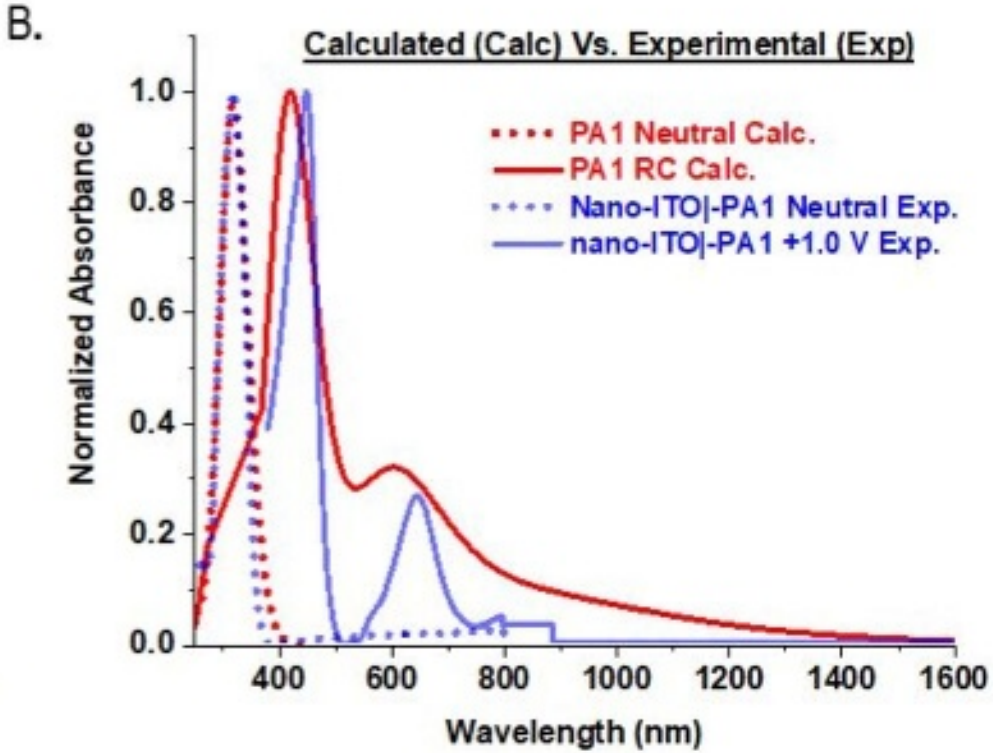
B.
Calculated (Calc) Vs. Experimental (Exp)
PA1 Neutral Calc.
PA1 RC Calc.
Nano-ITO|-PA1 Neutral Exp.
nano-ITO|-PA1 +1.0 V Exp.
Normalized Absorbance
Wavelength (nm)

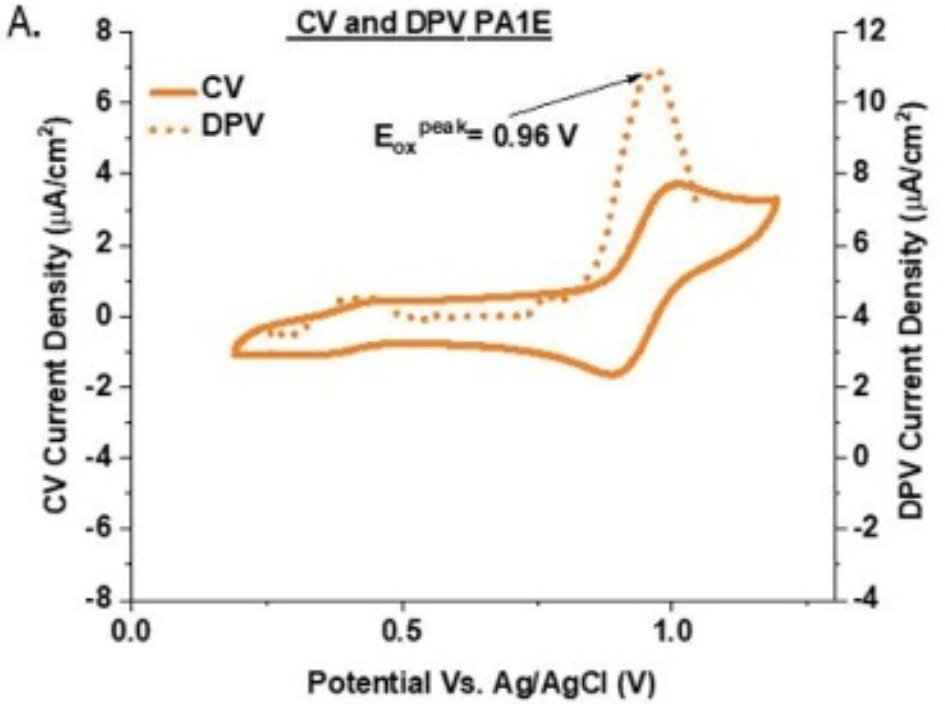
A.
CV and DPV PA1E
CV
DPV
E_{ox}^{peak}= 0.96 V
CV Current Density (μA/cm²)
DPV Current Density (μA/cm²)
Potential Vs. Ag/AgCl (V)

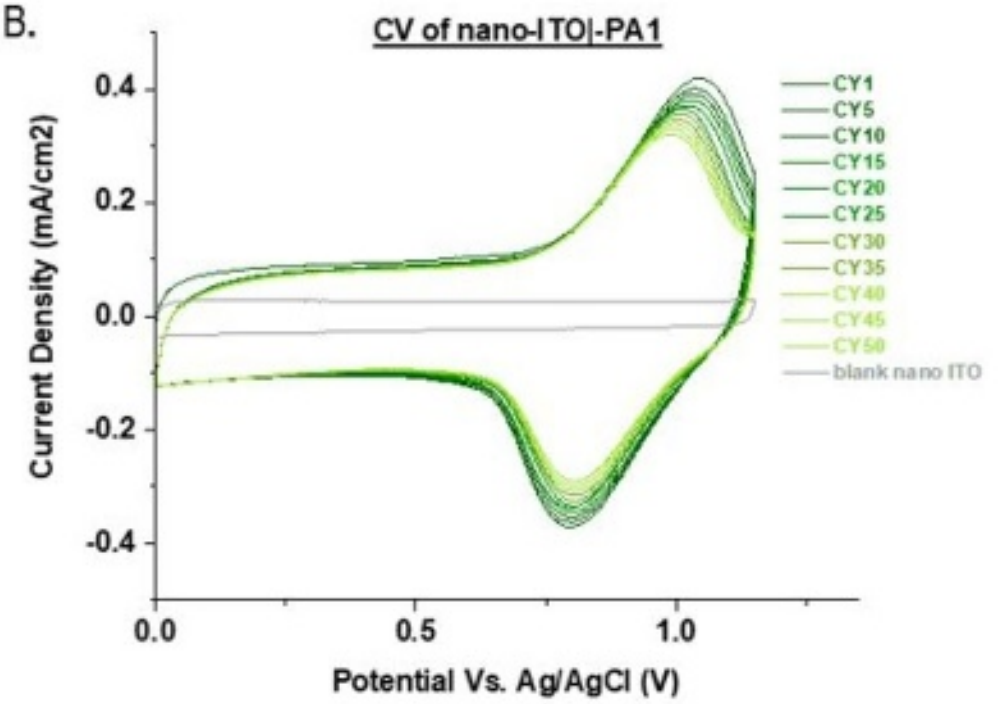
B.
CV of nano-ITO|-PA1
CY1
CY5
CY10
CY15
CY20
CY25
CY30
CY35
CY40
CY45
CY50
blank nano ITO
Current Density (mA/cm2)
Potential Vs. Ag/AgCl (V)

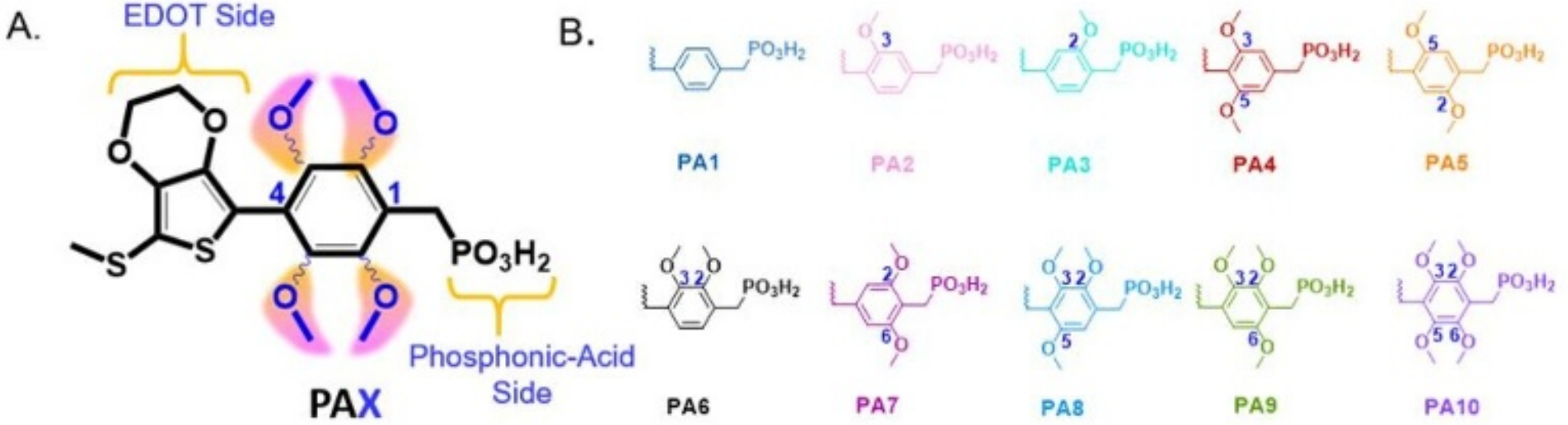
A.
EDOT Side
PO3H2
Phosphonic-Acid Side
PAX
B.
PA1
PA2
PA3
PA4
PA5
PA6
PA7
PA8
PA9
PA10

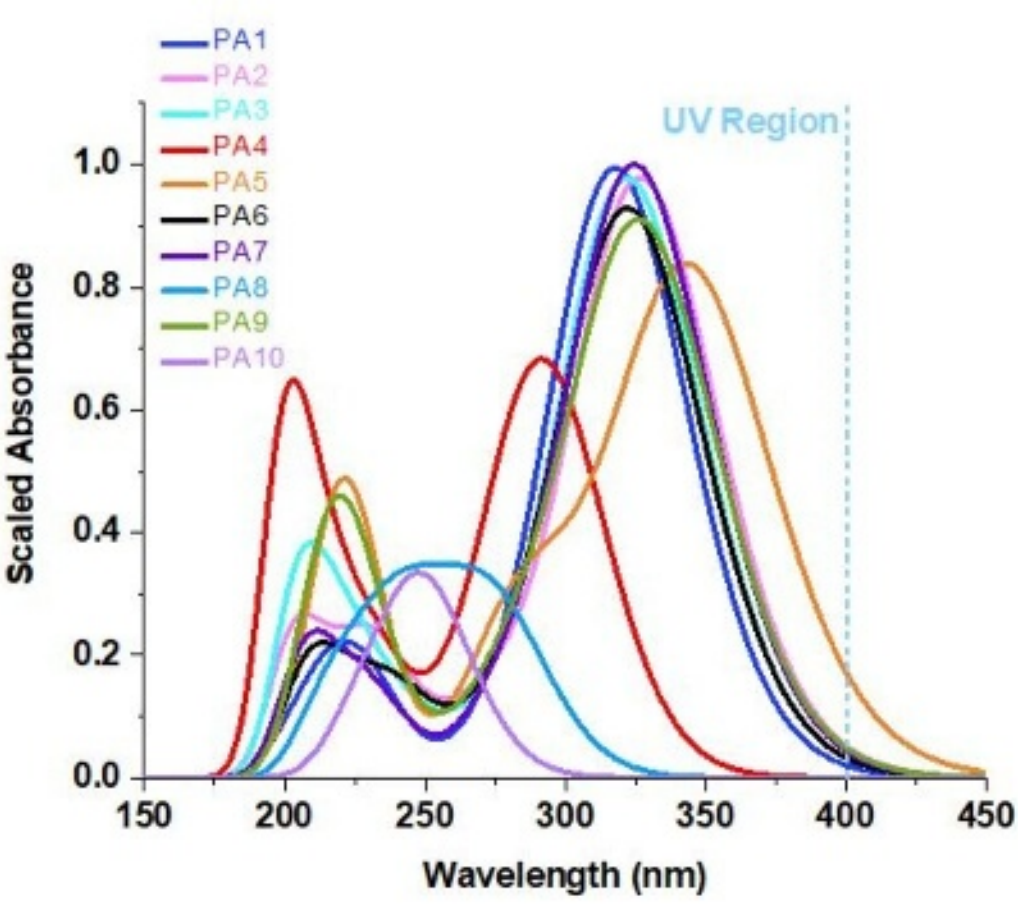
PA1
PA2
PA3
PA4
PA5
PA6
PA7
PA8
PA9
PA10
UV Region
Scaled Absorbance
1.0
0.8
0.6
0.4
0.2
0.0
150
200
250
300
350
400
450
Wavelength (nm)

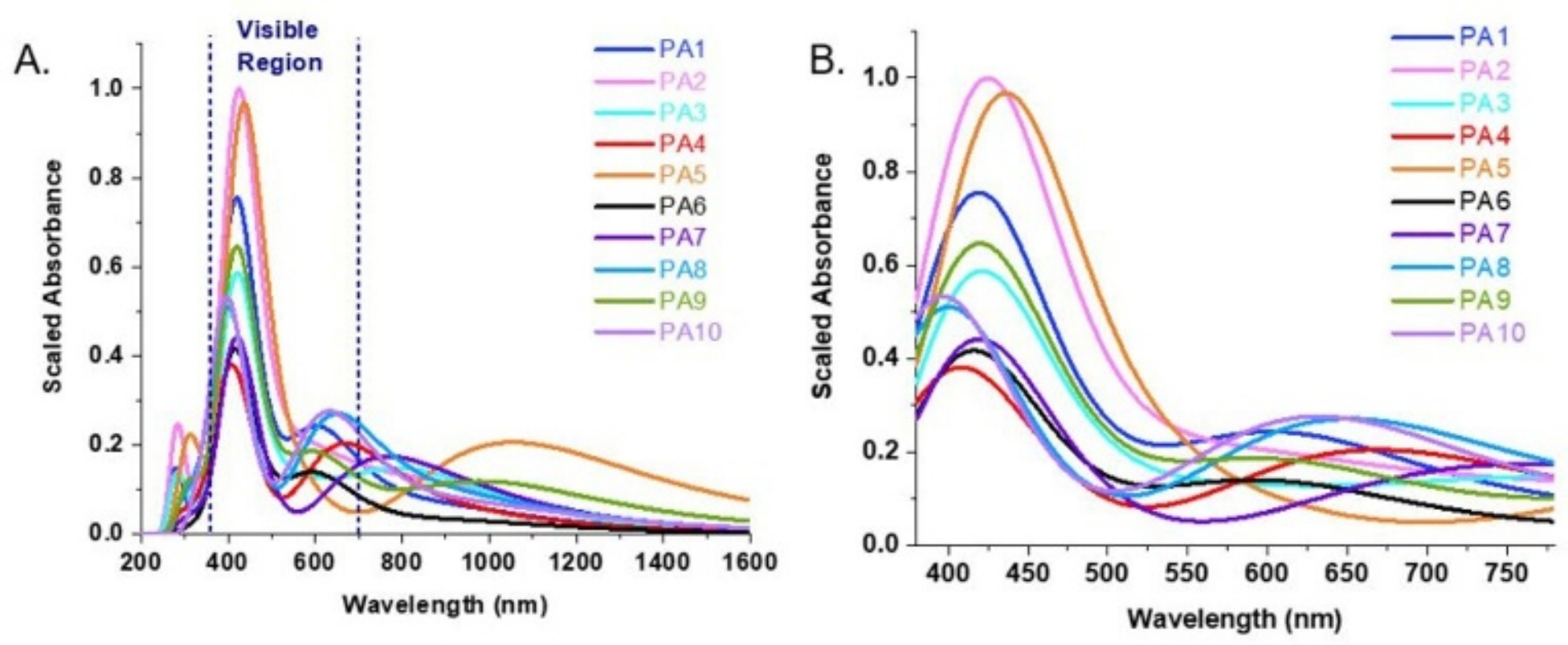
A.
Visible
Region
Scaled Absorbance
Wavelength (nm)
PA1
PA2
PA3
PA4
PA5
PA6
PA7
PA8
PA9
PA10
B.
Scaled Absorbance
Wavelength (nm)
PA1
PA2
PA3
PA4
PA5
PA6
PA7
PA8
PA9
PA10

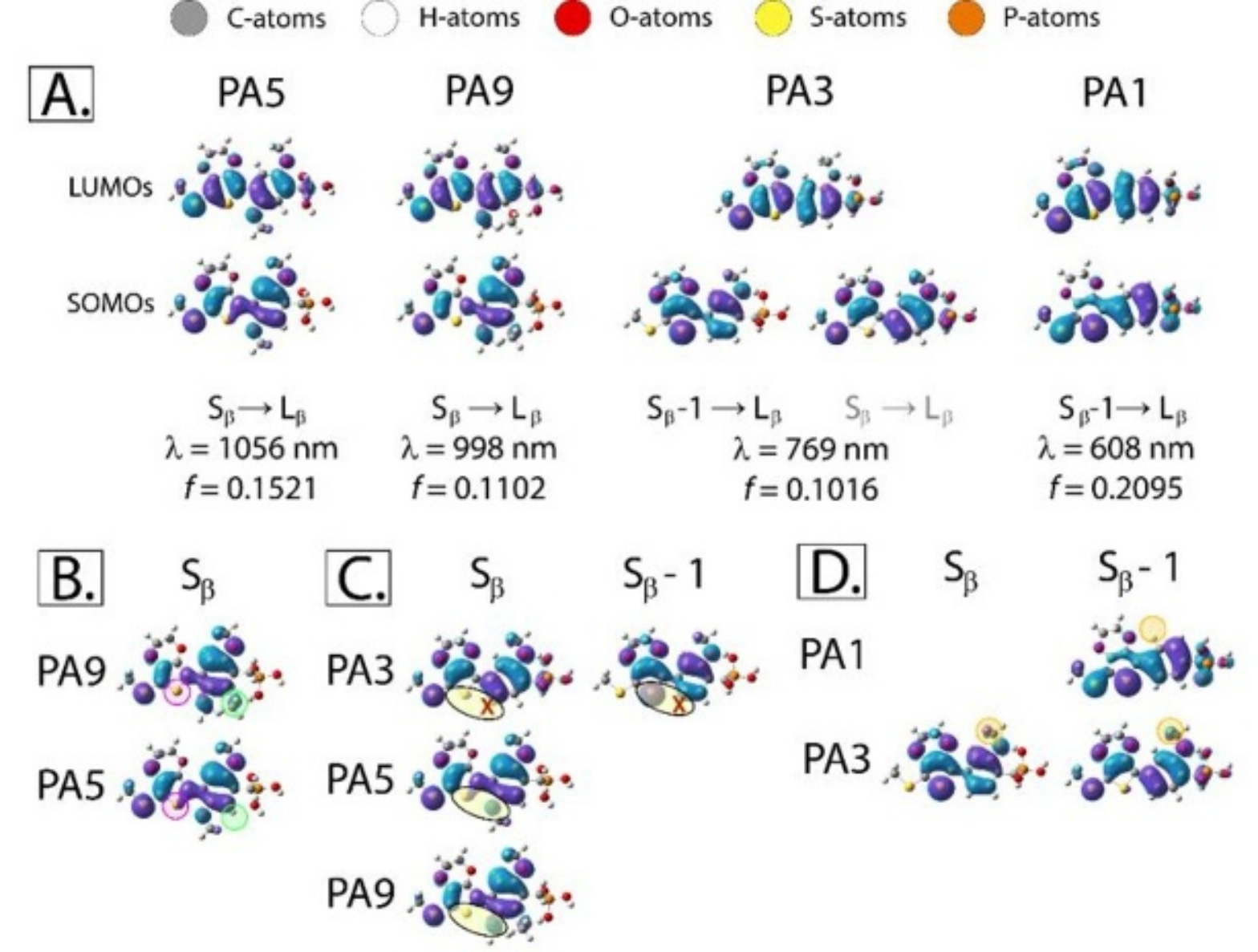
C-atoms
H-atoms
O-atoms
S-atoms
P-atoms
A.
PA5
PA9
PA3
PA1
LUMOs
SOMOs
$S_\beta \rightarrow L_\beta$
$\lambda = 1056$ nm
$f = 0.1521$
$S_\beta \rightarrow L_\beta$
$\lambda = 998$ nm
$f = 0.1102$
$S_\beta\text{-}1 \rightarrow L_\beta$
$S_\beta \rightarrow L_\beta$
$\lambda = 769$ nm
$f = 0.1016$
$S_\beta\text{-}1 \rightarrow L_\beta$
$\lambda = 608$ nm
$f = 0.2095$
B.
S_β
PA9
PA5
C.
S_β
S_β - 1
PA3
PA5
PA9
D.
S_β
S_β - 1
PA1
PA3